

1 **How PTEN mutations degrade function at the membrane and**
2 **life expectancy of carriers of mutations in the human brain**

3

4 Hyunbum Jang¹, Jiaye Chen², Lilia M Iakoucheva^{2,3}, Ruth Nussinov^{1,4,*}

5

6 ¹Computational Structural Biology Section, Frederick National Laboratory for Cancer
7 Research in the Cancer Innovation Laboratory, National Cancer Institute, Frederick, MD
8 21702, U.S.A.

9 ²Department of Psychiatry, University of California San Diego, La Jolla, CA 92093,
10 U.S.A.

11 ³Institute for Genomic Medicine, University of California San Diego, La Jolla, CA 92093,
12 U.S.A.

13 ⁴Department of Human Molecular Genetics and Biochemistry, Sackler School of
14 Medicine, Tel Aviv University, Tel Aviv 69978, Israel

15

16 * Corresponding Author

17

18 Correspondence should be addressed to:

19 Ruth Nussinov

20 Frederick National Laboratory for Cancer Research

21 Frederick, MD 21702, U.S.A.

22 Phone: 301-846-5579

23 E-mails: NussinoR@mail.nih.gov

24

25 **Abstract**

26 PTEN dysfunction, caused by loss of lipid phosphatase activity or deletion, promotes pathologies,
27 cancer, benign tumors, and neurodevelopmental disorders (NDDs). Despite efforts, exactly how
28 the mutations trigger distinct phenotypic outcomes, cancer or NDD, has been puzzling. It has also
29 been unclear how to distinguish between mutations harbored by isoforms, are they cancer or
30 NDDs-related. Here we address both. We demonstrate that PTEN mutations differentially
31 allosterically bias P-loop dynamics and its connection to the catalytic site, affecting catalytic
32 activity. NDD-related mutations are likely to sample conformations present in the wild-type, while
33 sampled conformations sheltering cancer-related hotspots favor catalysis-prone conformations,
34 suggesting that NDD mutations are weaker. Analysis of isoform expression data indicates that if
35 the transcript has NDD-related mutations, alone or in combination with cancer hotspots, there is
36 high prenatal expression. If no mutations within the measured days, low expression levels. Cancer
37 mutations promote stronger signaling and cell proliferation; NDDs' are weaker, influencing brain
38 cell differentiation. Further, exon 5 is impacted by NDD or non-NDD mutations, while exon 7 is
39 exclusively impacted by NDD mutations. Our comprehensive conformational and genomic
40 analysis helps discover how same allele mutations can foster different clinical manifestations and
41 uncovers correlations of splicing isoform expression to life expectancy.

42

43 **Key words:** tumor suppressor, glioblastoma, PTEN hamartoma tumor syndrome,
44 neurodevelopmental disorders, autism spectrum disorder, allostery, BrainSpan

45

46 Introduction

47 Tumor suppressor phosphatase and tensin homologue (PTEN) acts as a dual-specific protein and
48 lipid phosphatase, suppressing cell growth and survival (Tu et al., 2020). A major role of PTEN is
49 the negative regulation of phosphoinositide 3-kinase (PI3K)/phosphoinositide-dependent protein
50 kinase 1 (PDK1)/protein kinase B (AKT)/mammalian target of rapamycin (mTOR) signaling
51 through dephosphorylation of the signaling lipid phosphatidylinositol 3,4,5-trisphosphate (PIP₃)
52 to phosphatidylinositol 4,5-bisphosphate (PIP₂) (Georgescu, 2010). Dysfunction of PTEN due to
53 somatic and germline genetic variations is associated with many different disease phenotypes.
54 While somatic mutation of PTEN after conception is often associated with human cancers
55 including glioblastomas and endometrial carcinomas (Koboldt et al., 2021; Sansal and Sellers,
56 2004), germline mutations (in egg or sperm cells) lead to neurodevelopmental disorders (NDDs)
57 such as macrocephaly/autism syndrome (OMIM # 605309) (Busch et al., 2019; Morris-Rosendahl
58 and Crocq, 2020) and PTEN hamartoma tumor syndrome (PHTS) (Abkevich et al., 1995). PHTS
59 is a rare inherited syndrome characterized by a benign noncancerous tumor-like cell growth,
60 including Cowden syndrome (CS) and Bannayan-Riley-Ruvalcaba syndrome (BRRS) (Cummings
61 et al., 2022; Pilarski et al., 2013). Individuals with CS and BRRS often have macrocephaly, a non-
62 tumoural phenotype. Further, individuals with PHTS genetic disorder have increased risk for
63 certain types of cancer and autism spectrum disorder (ASD) (Butler et al., 2005; Buxbaum et al.,
64 2007; Tan et al., 2012; Yehia et al., 2022).

65 The *PTEN* gene encodes the second most frequently mutated protein in human cancer
66 followed by *TP53* (Yin and Shen, 2008). The most common PTEN mutations are nonsense,
67 frameshift, and deletion/insertion (Bonneau and Longy, 2000). They likely result in premature
68 termination of translation, which would decrease the level of PTEN protein in the cell. In addition,

69 a considerable number of PTEN mutations are missense point substitutions (Serebriiskii *et al.*,
70 2022) that may result in loss of protein function including reduced catalytic activity and protein
71 stability at the membrane. Missense mutations including indel mutations are commonly located at
72 the phosphatase domain, while nonsense mutations including truncation and frameshift are largely
73 found in the C2 domain (Bonneau and Longy, 2000; Serebriiskii *et al.*, 2022). In addition to the
74 mutations, posttranslational modifications (PTMs) on the C-terminal tail through the
75 phosphorylation of Ser/Thr cluster (Ser380, Thr382, Thr383, and Ser385) (Figure 1A) hamper
76 PTEN’s cellular membrane localization, silencing its catalytic activity (Bolduc *et al.*, 2013;
77 Dempsey *et al.*, 2021; Henager *et al.*, 2016). In human malignancies, premature terminations,
78 missense and nonsense mutations, frameshift mutations with frame deletion, PTMs including
79 phosphorylation, ubiquitination, oxidation of active-site, and acetylation elevate uncontrolled
80 PI3K-stimulated cell growth and survival (Alvarez-Garcia *et al.*, 2019; Kotelevets *et al.*, 2020;
81 Meng *et al.*, 2016; Singh and Chan, 2011; Song *et al.*, 2012; Xia *et al.*, 2020; Xu *et al.*, 2014; Zhang
82 *et al.*, 2020).

83 Although a number of experimental studies have demonstrated loss of PTEN lipid
84 phosphatase activity due to mutations, mechanistic details of the mutations and the structural
85 features of the mutant proteins at atomic resolution are still unknown. Here, comprehensive
86 computational studies using molecular dynamics (MD) simulations were performed for PTEN
87 mutants at an anionic lipid bilayer, composed of the phospholipids, phosphatidylcholine (PC) and
88 phosphatidylserine (PS), and the phosphoinositides, PIP₂ and PIP₃ (Figure 1B). We only
89 considered PTEN with the missense point substitutions, since proteins with the nonsense mutations
90 and premature terminations are not amenable to MD simulations. Eight missense mutations of
91 PTEN were considered: six in the phosphatase (Y68H, H93R, A126T, R130Q, G132D, and R173C)

92 and two in the C2 (F241S and D252G) domains (Figure 1C). The types of mutations selected for
93 the residues were with different chemical properties, ensuring that structural integrity of protein
94 can be observable due to the mutations within the simulation time. Among them, Y68H is in the
95 core of phosphatase domain and H93R is in the WPD loop (residues 88-98). The A126T, R130Q,
96 and G132D mutations occur in and near the P loop (residues 123-130) with the catalytic signature
97 motif, $^{123}\text{H}\text{CxxGxxR}^{130}$ (where x is any amino acid). R173C is located at the interface between the
98 phosphatase and C2 domains. For the C2 mutations, F241S is in the β -sandwich of the C2 domain
99 and D252G is located at the interface between two major domains. Our studies indicate that the
100 PTEN mutants can effectively absorb the anionic lipid bilayer, similar to wild-type PTEN.
101 However, the mutations significantly reduce protein stability and hinder substrate recruitment. The
102 dynamics of the P loop were restrained due to the strong allosteric signals from the mutation sites,
103 which would affect the PTEN's catalytic activity.

104 Our results underscore the merit of detailed structural and functional mechanisms of PTEN
105 with mutations at the membrane, point how they may help resolve the enigma of how same-protein
106 mutations can promote different pathologies, cancer versus NDDs, and a way to help determine
107 their outcome. The sampled conformations of mutants harboring a mutation associated with an
108 NDD resemble those of the wild-type protein. In contrast, conformations sampled by variants
109 associated with cancer hotspots differ and indicate more potent catalytic activation. This supports
110 the hypothesis that a key difference between cancer and NDDs mutations is mutation strength
111 (Nussinov et al., 2022b; c). A strong activating mutation promotes cell proliferation, a weak/mild
112 mutation promotes differentiation. This suggests that mutation strength, as manifested in the biased
113 conformational sampling that the mutant favors can be harnessed as a feature in identifying

114 mutations connected with the distinct clinical manifestation, cancer or NDD, assisting in early
115 diagnosis.

116 NDDs emerge during embryonic brain cell development, suggesting that in addition to
117 mutations, the level of prenatal gene expression plays a vital role. We analyzed prenatal and
118 postnatal expression levels of isoforms harboring NDD (macrocephaly/ASD)-related mutations
119 alone or in combination with cancer mutations. All mutant-harboring isoforms were highly
120 expressed in the prenatal time window, dropping following birth; if no mutations within the
121 measured life span, lower prenatal expression. Cancer development results from multiple (more
122 than one hotspot) mutations, emerging sporadically during life. NDDs mutation carriers have
123 higher chances of cancer emergence, suggesting that NDDs-related mutations can combine with
124 cancer mutations. If they reside at adjacent chromosomal regions, deletions/insertions can also
125 infringe both.

126 Our analysis helps learning how same allele mutations can abet different clinical
127 manifestations and uncovers correlations of splicing isoform expression with life expectancy. It
128 observes that splicing isoforms that do not carry exon 5 are exclusively impacted by the NDD
129 mutations, F241S and D252G. On the other hand, variants carrying exons 5 and 7 can be highly
130 correlated with increased lifetime risk for certain types of cancer. Individuals afflicted with NDDs
131 are known to have increased risk of cancer, in schizophrenia as much as 50% probability
132 (Nordentoft et al., 2021). It is also high in e.g., autism (Liu et al., 2022a), and in intellectual
133 disability (Achterberg et al., 1978; Liu et al., 2021). Our work also offers guidelines for
134 identification of cancer and NDD mutational variants. If the transcript harbors unknown mutation
135 types, they can be differentiated by their strengths; cancer mutations tend to be stronger, with
136 higher signaling levels; NDD's weaker, with moderate signaling. To differentiate between the

137 mutations, statistics and atomistic simulations can help, although applying MD on a large scale is
138 demanding. Sampling could be accelerated. However, the challenge in accelerated conformational
139 sampling is to have it sensitive to sequence alterations.

140

141 **Results**

142 A full-length PTEN contains 403 amino acids (Lee et al., 1999), consisting of the N-terminal PIP₂-
143 binding domain (PBD, residues 1-15), the phosphatase domain (residues 16-185), the C2 domain
144 (residues 190-350), and the carboxy-terminal tail (CTT, residues 351-403) (Figure 1). The CTT
145 includes the PDZ binding motif (PDZ-BM, ⁴⁰¹TKV⁴⁰³) at the C-terminal end. For catalysis, the
146 phosphatase domain provides three critical catalytic residues in the active site; Asp92 in the WPD
147 loop, and Cys124 and Arg130 in the P loop. We performed MD simulations on eight different
148 PTEN mutants interacting with an anionic lipid bilayer composed of PC, PS, PIP₂, and PIP₃. The
149 initial configuration of PTEN mutants at the membrane is the “open-open” conformation (Malaney
150 et al., 2013; Rahdar et al., 2009; Ross and Gericke, 2009), reflecting the relaxed PTEN
151 conformation at the anionic lipid bilayer as observed in the wild-type case (Jang et al., 2021; Nanda
152 et al., 2015; Shenoy et al., 2012). All PTEN mutants stably anchored in the anionic lipid bilayer.
153 As observed in the wild-type PTEN system with the same lipid compositions (Jang et al., 2021),
154 the probability distribution functions of membrane contacts of the protein residues point to five
155 loops that are responsible for the membrane association (Figure 1—figure supplement 1). The peaks
156 in the distribution indicate PBD-p β 1(¹⁹DGF Δ L²³) and p β 2-p α 1 (⁴¹RLEGVYR⁴⁷) loops in the
157 phosphatase domain, and c β 1-c β 2 (²⁰⁵MFSGGTC²¹¹), CBR3 (²⁶⁰KQNKMLKKDK²⁶⁹), and Ca2
158 (³²⁷KANKDKANR³³⁵) loops in the C2 domain. In addition to the PBD, the two positively charged
159 loops, p β 2-p α 1 and CBR3 loops, one from the phosphatase domain and the other from the C2

160 domain, are major membrane-binding interfaces of PTEN mutants. As observed in the wild-type
161 systems, similar profiles of the distributions of the helix tilt angles for the helices in the
162 phosphatase domain of PTEN mutants (Figure 1–figure supplement 2) suggest that membrane
163 absorption and orientation of the protein are highly affected by the lipid compositions in the bilayer.

164

165 **Y68H in the core of phosphatase domain**

166 In wild-type PTEN, Tyr68 in p β 3 forms an aromatic cluster with Tyr88 in p β 4 and Phe104 in p α 3.
167 In the Y68H mutant, the point substitution disrupts this cluster (Figure 2A), resulting in the
168 destruction of the salt bridge between Lys66 in p β 3 and Asp107 in p α 3 (Figure 2B). The membrane
169 absorption of the p β 2-p α 1 loop in the phosphatase domain seems to be weaker than that of the
170 other mutants and wild-type system (Figure 1–figure supplement 1). The disruptions of key residue
171 interactions cause a conformational change in the phosphatase domain, yielding a loosely packed
172 core structure. This provides room for the mutant residue His68 to rotate its aromatic ring. The
173 periodic fluctuations in the distance between HD1 at the ring and HB2 at C β atom indicate the
174 rotation of His68 aromatic sidechain (Figure 2C). In comparison with wild-type PTEN, no rotation
175 of the aromatic ring of Tyr68 is monitored. To observe how the mutation allosterically affects the
176 conformation of the active site, we identified the signal propagation pathways through the protein
177 by calculating the dynamic correlated motion among residues using the weighted implementation
178 of suboptimal paths (WISP) algorithm (Van Wart et al., 2014). A number of optimal and
179 suboptimal pathways were generated between the source residue, His68 (or Tyr68 for wild type),
180 and the sink residues, Cys124 and Arg130, in the P loop (Figure 2D). The allosteric signal
181 propagations through the protein illustrate that the mutant residue His68 is dynamically correlated
182 with the P loop residues, Cys124, Lys125, Arg130, and Thr131. The strong allosteric signals due

183 to the mutation transmitting through the active site constrain the P loop to move upwards from the
184 bilayer surface (Figure 2E). In marked contrast to the mutant system, the allosteric signal nodes of
185 Lys125 and Thr131 are absent in the signal propagation pathways from the wild-type residue
186 Tyr68, implicating weak allosteric coupling to the P loop. For Y68H, the allosteric restraint on the
187 P loop with the shifted conformation hampers the catalytic residue Arg130 recruitment of the
188 substrate PIP₃ (Figure 2F), which can lead to reduced catalytic activity.

189

190 **H93R in the WPD loop**

191 The P loop is highly basic, containing three basic residues that facilitate the recruitment of the
192 acidic substrate PIP₃ to the catalytic pocket. For catalysis, three catalytically significant residues,
193 Cys124 and Arg130 in the P loop and Asp92 in the WPD loop, align to coordinate PIP₃ at the
194 active site. The WPD loop in a closed conformation can bring Asp92 in the coordination, leading
195 to high catalytic activity (Brandao et al., 2012). A point substitution H93R in the WPD loop
196 amplifies the positively charged nature of the active site (Figure 3). The location of the WPD loop
197 with respect to the P loop is comparable to the wild type (Figure 3–figure supplement 3),
198 suggesting that H93R preserves the closed loop conformation. However, the mutant residue Arg93
199 increases the interaction with the substrate PIP₃, which seems to block the migration of the substrate
200 to the catalytic site residues. This additional membrane interaction might be correlated with the
201 absence of the membrane contact of the Cα2 loop in the C2 domain (Figure 1–figure supplement
202 1A).

203

204 **A126T, R130Q, and G132D in the P loop**

205 The P loop contains the catalytic signature motif $^{123}\text{HCKAGKGR}^{130}$, suggesting that any mutation
206 of P loop residue can alter the loop conformation. Our data illustrate that the direct P loop
207 mutations, A126T and R130Q, and G132D nearby the P loop, induce a collapsed loop
208 conformation (Figure 4A). In contrast, it was found that an extended (or relaxed) conformation of
209 the P loop is populated for wild-type PTEN when the anionic bilayers contain both PIP₂ and PIP₃
210 (Jang *et al.*, 2021). Although our mutant systems contain the same phosphoinositide lipids, they
211 yield the collapsed P loop conformation regardless of the lipid composition. Interestingly, both
212 A126T and R130Q mutants show an open conformation of the WPD loop with increased distance
213 from the P loop as compared to the wild type (Figure 4B). However, the G132D mutant maintains
214 a closed conformation of the WPD loop with the distance from the P loop comparable to wild-type
215 PTEN, suggesting that G132D exhibits weaker mutational effect compared to the other mutations.

216 For catalysis, PTEN requires residual water molecules around the sidechains of Cys124
217 and Arg130 at the active site in the process of hydrolysis to release the phosphate group from
218 Cys124 after transferring it from PIP₃ (Brandao *et al.*, 2012). To delineate the catalytic activity in
219 the mutant systems, we calculated the three-dimensional water density map in the region of the
220 phosphatase domain (Figure 5). Compared to the wild-type system, low probability of water
221 around the catalytic residues indicates that the active sites of A126T, R130Q, and G132D mutants
222 are largely dehydrated. The severe dehydration in the active site of R130Q suggests that the
223 mutational effect may be stronger than the other mutants. For R130Q, changes in the helix tilt
224 angles for $\text{p}\alpha 3$ and $\text{p}\alpha 5$ are apparent when compared to wild-type PTEN (Figure 1–figure
225 supplement 2A).

226

227 **R173C at the interface**

228 In wild-type PTEN, Arg173 in p α 6 of the phosphatase domain is important for maintaining the
229 interdomain interaction at the interface between the phosphatase and C2 domains. It forms a strong
230 salt bridge with Asp324 in the c β 7-c α 2 loop, which induces the interdomain π - π stacking between
231 Tyr177 in p α 6 and Phe279 in c α 1 (Figure 6A). In the R173C mutant, the absence of the salt bridge
232 actuates the destabilization of the interface, resulting in the disruption of the π - π stacking. The
233 removal of these key residue interactions increases the interdomain distance at the mutation site
234 (Figure 6B). However, the opposite site of the interface is still maintained by the hydrophobic
235 interaction between Pro95 in the WPD loop and Trp274 in c β 6, and an additional salt bridge
236 formation between Gln97 in the WPD loop and Asp252 in c β 5. This unbalanced interaction in the
237 interface induces the rotation of the C2 domain with respect to the phosphatase domain (Figure
238 6C), causing the loss of the membrane contact of the C α 2 loop in the C2 domain (Figure 1–figure
239 supplement 1A). The allosteric signaling pathways from the mutant residue Cys173 to the catalytic
240 residue Arg130 seem to be stronger than those from the wild-type residue Arg173 (Figure 6D).
241 This suggests that the R173C mutant allosterically constrains the P loop through the multiple
242 shortest optimal pathways. The allosteric restraint on the P loop changes the loop conformation
243 that moves upwards from the bilayer surface as observed in Y68H (Figure 6E). The shifted P loop
244 that the location is highly elevated from the bilayer surface and adopts a collapsed loop
245 conformation (Figure 6F), which induces the WPD loop open conformation. We observed that the
246 substrate PIP₃ is populated in the region of the C2 domain. The failure of the R173C mutant to
247 recruit PIP₃ by Arg130 (Figure 6G) indicates that it has a reduced catalytic activity.

248

249 **F241S and D252G in the C2 domain**

250 F241S in c β 4 resides in the pocket of the β -sandwich of the C2 domain, forming a hydrophobic
251 cluster. D252G in c β 5 occurs at the interface between the phosphatase and C2 domains, similar to
252 R173C. As expected, both C2 mutations increase the fluctuations in the C2 domain as compared
253 to wild-type PTEN (Figure 7A). However, averaged deviations of the key basic residues from the
254 bilayer surface are markedly different between these two C2 mutants (Figure 7B). The profile of
255 averaged deviations of F241S resembles that of wild-type PTEN, but that of D252G is distinct.
256 F241S shows a relatively weak membrane absorption of the p β 2-p α 1 loop (Figure 1–figure
257 supplement 1B), and D252G alters the helix tilt angles for the helices in the phosphatase domain
258 (Figure 1–figure supplement 2B). F241S destabilizes the hydrophobic core of the β -sandwich
259 (Figure 7C), affecting the dynamic correlations of motions of the residues in the C2 domain. The
260 allosteric signal propagations from the mutant residue Ser241 to the active site avoid the signal
261 nodes in the hydrophobic core, while the allosteric signals from the wild-type residue Phe241
262 transmit through the signal nodes in the hydrophobic core of the β -sandwich (Figure 7D). F241S
263 obtains a single optimal pathway that passes more allosteric signal nodes than the wild type,
264 indicating less effective allosteric connection to the active site. In contrast, D252G exhibits strong
265 allosteric connection to the active site (Figure 7E). The allosteric signals from the wild-type residue
266 Asp252 propagate through the signal nodes at the interface, Pro95 and Trp274, and in the WPD
267 loop, Glu91, Asp92, His93, Asn94, and Pro96. However, the allosteric signals transmitting through
268 the WPD loop is missing in the D252G mutant. The loss of the hydrophobic interaction due to the
269 mutation destabilizes the interface (Figure 7F) and increases the interfacial distance (Figure 7G).
270 D252G shows the similar behavior as observed in R173C since both mutations occur in the same
271 interface but in different side.

272

273 **PTEN variants expressions for NDD vs. non-NDD**

274 PTEN mutations are associated with various diseases including PHTS, cancer, and NDDs. Some
275 PTEN mutations are exclusively expressed in a certain disease type, but mutations can share across
276 both disease phenotypes. Here, the NDD-related mutations are H93R, F241S, and D252G that are
277 exclusively responsible for macrocephaly/autism syndrome (Butler *et al.*, 2005). The *PTEN* gene
278 is located on the chromosome 10 and contains nine exons. The longest human PTEN splicing
279 isoform is encoded by the transcript ENST00000371953, with exon 3 (Y68H) and exon 6 (R173C)
280 being impacted by the non-NDD mutations, exon 7 (F241S and D252G) by the NDD mutations,
281 and exon 5 (H93R, A126T, R130Q, and G132D) by both, the NDD and non-NDD mutations
282 (Figure 8A).

283 Two other transcripts (ENST00000498703 and ENST00000472832) are shorter isoforms
284 that carry above combinations of mutations, except that exon 6 in the ENST00000472832 isoform
285 (87952199-87952259, GRCh38.p13) is slightly (~80 bp) shorter than the same exon in the
286 ENST00000371953 isoform (87952118-87952259, GRCh38.p13) due to alternative splicing, and
287 it therefore carries only two NDD mutations in its exon 7 (F241S and D252G) and is missing a
288 non-NDD mutation R173C from exon 6. There are additional isoforms comprising exons 1 and 2
289 that do not carry any known disease risk mutations. We quantified expression levels of these five
290 isoforms from the RNA-seq dataset of the developing human brain BrainSpan (Kang *et al.*, 2011;
291 Li *et al.*, 2018), as we have previously described (Chau *et al.*, 2021), and observed that three PTEN
292 isoforms (ENST00000371953, ENST00000472832, and ENST00000498703) are highly
293 expressed prenatally, and their expression levels decrease after birth (Figure 8B). The remaining
294 two isoforms (ENST00000487939 and ENST00000462694) that are not impacted by mutations,
295 are lowly expressed in the developing brain. Interestingly, the isoform ENST00000472832 with

296 the shorter exon 6 that is exclusively impacted only by the NDD mutations, is the second highly
297 expressed PTEN isoform, which may have further implications for NDD biology.

298

299 **Discussion**

300 Here, we considered six PTEN mutations in the phosphatase domain (Y68H, H93R, A126T,
301 R130Q, G132D, and R173C) and two in the C2 domain (F241S and D252G). Our studies
302 demonstrate that the PTEN mutants retain the wild-type capability of the membrane absorption to
303 the anionic lipid bilayer (Han *et al.*, 2000). However, the dynamics of the P loop, the WPD loop
304 conformation, the hydration of the active site, and the substrate recruitment were greatly affected
305 by the mutations. Y68H is associated with CS, BRRS, and glioblastoma, which is known to be
306 affected by the loss of phosphatase activity and protein stability (Han *et al.*, 2000; He *et al.*, 2011;
307 Marsh *et al.*, 2001; Post *et al.*, 2020; Tsou *et al.*, 1998). In our simulations, Y68H disrupted the
308 core of the phosphatase domain and allosterically constrained the P loop, which hinders the
309 recruitment of the substrate PIP₃. The NDD-related mutation H93R is responsible for
310 macrocephaly/autism syndrome, displaying a modest loss of catalytic activity (Fricano-Kugler *et*
311 *al.*, 2018; Redfern *et al.*, 2010; Rodriguez-Escudero *et al.*, 2011). In our structural model, H93R in
312 the WPD loop hijacked the substate PIP₃, interrupting the catalytic site residues recruitment of the
313 substate for catalysis. But the mutant protein preserved the closed WPD loop conformation. For
314 the P loop mutations, A126T is found in endometrial and ovarian carcinomas (Valtcheva *et al.*,
315 2017), and R130Q is shared by CS and endometrial carcinoma (Han *et al.*, 2000; Serebriiskii *et*
316 *al.*, 2022). In our simulations, these mutations yielded a collapsed conformation of the P loop,
317 resulting in the loss of contact with the WPD loop. G132D near the P loop, which is associated
318 with endometrial carcinoma and ASD (Chao *et al.*, 2020; Post *et al.*, 2020), also exhibited the

319 collapsed P loop conformation but preserved the closed WPD loop conformation. We observed
320 that the PTEN mutations in the P loop, or nearby, cause dehydration in the active site, where water
321 molecules are important for hydrolysis to release the phosphate group from the active site (Brandao
322 *et al.*, 2012). R130Q exhibited more severe dehydration than the other mutants. At the interface
323 between the phosphatase and the C2 domains, R173C is associated with cancer, such as
324 glioblastoma and endometrial carcinoma (Han *et al.*, 2000; Shan *et al.*, 2020). We found that
325 R173C disrupts the domain-domain interaction, allosterically biasing the P loop dynamics. Similar
326 behavior was observed for the C2 mutation D252G at the interface. However, the other C2
327 mutation, F241S in the β -sandwich of C2 domain, exhibited less effective allosteric connection to
328 the catalytic site than that observed in wild-type PTEN. Both NDD-related C2 mutations F241S
329 and D252G are responsible for macrocephaly/autism syndrome (Fricano-Kugler *et al.*, 2018;
330 Mingo *et al.*, 2018; Post *et al.*, 2020; Rodriguez-Escudero *et al.*, 2011; Spinelli *et al.*, 2015).

331 Total loss of protein function can occur when PTEN has: (i) reduced protein expression
332 due to truncation and (ii) PTM, i.e., C-terminal tail phosphorylation in solution. In these cases,
333 PTEN is totally removed from the cell membrane, dismissing its catalytic activity (Bolduc *et al.*,
334 2013; Dempsey *et al.*, 2021; Henager *et al.*, 2016). On the other hand, PTEN with missense
335 mutations can effectively absorb the cell membrane, exhibiting function with reduced activity (Han
336 *et al.*, 2000). We characterized the structural integrity of how PTEN degrades its function at the
337 membrane due to missense mutations. Our membrane bound PTEN mutants exhibited key
338 structural features: (i) the phosphatase domain with reduced stability, (ii) the allosteric constraint
339 on the P loop, (iii) the collapsed P loop, (iv) the dehydration of active site, and (v) the open
340 conformation of WPD loop. Although the simulations cannot directly assay PTEN lipid
341 phosphatase activity, the failure in the coordination of the substrate PIP₃ at the catalytic residues is

342 a corollary of all the above structural features that lead to silencing PTEN catalytic activity. The
343 phosphatase mutations, Y68H, A126T, R130Q, and R173C have all the above structural features
344 induced by the mutations, suggesting that these proteins appear to exhibit a strong mutational effect.
345 In contrast, the NDD-related H93R and F241S exhibit a weak mutational effect with few structural
346 features by the mutations. Both cancer- and NDD-related G132D and only NDD-related D252G
347 exhibit an intermediate mutational effect with the structural features by the mutations.

348 In our studies, the phosphatase mutations are associated with cancer, PHTS, and NDDs,
349 while the C2 mutations are exclusively related to NDDs. Principal component analysis (PCA) of
350 the sampled conformations found that the macrocephaly and ASD related mutations, H93R and
351 F241S, favor sampling conformations present in wild-type PTEN (Figure 8–figure supplement 4).
352 In contrast, the sampled conformations for the cancer and PHTS-related mutations, Y68H, A126T,
353 and G132D, differ from those in wild-type PTEN. The interface mutations R173C and D252G
354 favor sampling similar conformations. Interestingly, although the sampled conformations for
355 R130Q can overlap those of the wild-type PTEN, the function of the mutant protein largely differs.
356 We suspect that a key structural effect of the PTEN missense mutation at the membrane is an
357 impact on the dynamics and conformation of the P loop. The strong PTEN mutations, Y68H and
358 R173C, which are distant from the active site, constrain the P loop through a strong allosteric
359 signal, while R130Q, the mutation directly on the P loop, strongly controls the loop conformation.
360 It was reported that cancer or PHTS-associated mutations targeting the P-loop of PTEN resulted
361 in complete loss of protein function (Rodriguez-Escudero *et al.*, 2011).

362 These distinct structural features in PTEN mutations appear to correlate with mutation
363 strength and timing of the expression of the transcripts that determine the cancer and NDD
364 outcomes. PTEN contains nine exons, and its mutations largely occur in exon 5, followed by exon

365 7, 3, and 6 (Tan et al., 2011). Most missense mutations occur within the phosphatase domain, while
366 the C2 domain mainly accommodates nonsense mutations. The largest exon 5 encodes the PTEN
367 residues 84-164 including the catalytic signature motif, $^{123}\text{H}\text{CxxGxxR}^{130}$. It was found that up to
368 40% of all germline mutations are located in exon 5 (Waite and Eng, 2002). The developing brain
369 isoform expression data indicate that exon 5 is impacted by NDD or non-NDD mutations.
370 Interestingly, we observed that PTEN splicing isoforms that do not carry exon 5 are exclusively
371 impacted by the NDD mutations, F241S and D252G. We expect that the increased life expectancy
372 of PTEN variants carrying exons 5 and 7 can be highly correlated to increased lifetime risk for
373 certain types of cancer.

374

375 **Conclusions**

376 PTEN, like other proteins in the signaling networks of the Ras superfamily and their associated
377 regulatory proteins harbor mutations connected with cancer and with NDDs. As a phosphatase,
378 PTEN is undruggable. Its associated interactome can be. Early diagnosis could help in ASD
379 pharmacology. Identifying the mutations acting in cancer, NDD, or both has been challenging. The
380 timing of the expression is a major determinant, during embryonic development or sporadic,
381 throughout life in cancer. Here our data suggest that mutation strength is another crucial factor. To
382 determine the mutation strength here we exploit the conformations sampled by the mutants. If the
383 conformations are biased toward the wild type, we interpret the mutation as low/mild, acting in
384 NDD. If they differ, adopting catalytically favored states, we label them as tending to strong
385 hotspots. Strong mutations result in a larger population of active molecules, thus stronger signals
386 reaching the cell cycle to promote proliferation (Nussinov et al., 2022a; d). We suggest sampling
387 as a general approach toward defining the likelihood of mutations to act in distinct pathology in

388 diagnosis. The atomistic MD simulations used here are limited by molecular size, and the number
389 of proteins and mutations. Accelerated MD can be applied on a broader scale. It could also be
390 employed as a first step in sequence sensitive, deep modeling (Strokach and Kim, 2022). We
391 expect that other proteins bearing NDD connected mutations also display biased conformations.

392 MD simulations are a powerful tool to gain insight into the molecular behavior of proteins,
393 wild type, and mutants. However, in the living cell, the conformational behavior is not stand-alone,
394 and the mutant behavior is insufficient in determining cell transformation (Nussinov *et al.*, 2022a;
395 d). In addition to the mutation strength, determinants of signal strength include mechanisms that
396 can block or enhance the signal, the types, and locations of additional mutations, and critically, the
397 expression levels of the respective isoforms, and of cross-talking proteins in the pathway that
398 regulate the protein variants. Signal levels vary across cell types, states, and time windows, with
399 chromatin structure and alternative splicing playing key roles. A strong activating mutation can be
400 constrained by low expression level, and a weak/moderate mutation can be strengthened by high
401 expression. Considering the spatio-temporal isoform expression in relevant tissues and cell types
402 in conjunction with mutations can help unravel the molecular mechanisms driving human disease.
403 Here, the expression levels of splicing isoforms harboring NDD, and mixed NDD/cancer
404 mutations are elevated at the prenatal stage, dropping following birth. The mapping of these
405 mutations on the respective exons and the presence of the exons in the isoforms, can be among the
406 factors foretelling life expectancy.

407

408 **Materials and methods**

409 **Construction of full-length PTEN protein with mutations**

410 To generate the initial configuration of full-length PTEN mutants, we adopted the conformations
411 of wild-type PTEN interacting with the membrane from previous studies (Jang *et al.*, 2021).
412 Explicit membrane simulations generated the fully relaxed wild-type proteins on an anionic lipid
413 bilayer composed of DOPC:DOPS:PIP₂:PIP₃ (32:6:1:1 molar ratio). The wild-type sequence was
414 modified to generate eight different PTEN mutants with each point mutation of Y68H, H93R,
415 A126T, R130Q, G132D, R173C, F241S, and D252G. The anionic lipid bilayer with the same lipid
416 compositions as in the wild-type system were reconstructed for the adopted mutant proteins. For
417 all mutant systems, the initial configuration ensured that the PBD, phosphatase domain, and C2
418 domain were placed on the top of the bilayer surface without inserting the protein backbone into
419 the bilayer, but the C-tail resided in bulky region without interacting with the lipid bilayer. Both
420 PBD and C-tail were modeled as unstructured chains.

421

422 **Atomistic molecular dynamics simulations**

423 MD simulations were performed on PTEN mutant systems using the updated CHARMM program
424 with the modified all-atom force field (version 36m) (Brooks *et al.*, 2009; Huang *et al.*, 2017;
425 Klauda *et al.*, 2010). Our computational studies closely followed the same protocol as in our
426 previous works (Grudzien *et al.*, 2022; Haspel *et al.*, 2021; Jang *et al.*, 2016a; Jang *et al.*, 2019;
427 Jang *et al.*, 2016b; Jang *et al.*, 2021; Jang *et al.*, 2020; Liao *et al.*, 2020; Liu *et al.*, 2022b; Liu *et*
428 *al.*, 2022c; Maloney *et al.*, 2021; Maloney *et al.*, 2022; Weako *et al.*, 2021; Zhang *et al.*, 2021a;
429 Zhang *et al.*, 2021b). Prior to production runs, a series of minimization and dynamics cycles were
430 performed for the solvents including ions and lipids with a harmonically restrained protein
431 backbone until the solvent reached 310 K. Next, preequilibrium simulations with dynamic cycles
432 were performed while gradually releasing the harmonic restraints on the backbones of PTEN

433 mutants. The particle mesh Ewald (PME) method was used to calculate the long-range electrostatic
434 interaction, and the van der Waals (vdW) interactions using switching functions with the twin
435 range cutoff at 12 Å and 14 Å were calculated for the short-range interaction between atoms. In
436 the production runs, the Nosé-Hoover Langevin piston control algorithm was used to sustain the
437 pressure at 1 atm, and the Langevin thermostat method was employed to maintain the constant
438 temperature at 310 K. The SHAKE algorithm was applied to constrain the motion of bonds
439 involving hydrogen atoms. Simulations were performed for eight mutant systems each with 1 μs,
440 and additional simulations for the same systems were also performed to check reproducibility. The
441 production runs were performed with the NAMD parallel-computing code (Phillips et al., 2005)
442 on a Biowulf cluster at the National Institutes of Health (Bethesda, MD). The result analysis was
443 performed in the CHARMM program (Brooks *et al.*, 2009). To determine the most populated
444 conformation, the ensemble clustering in Chimera (Pettersen et al., 2004) was implemented to
445 obtain the conformational representatives. The weighted implementation of suboptimal path
446 (WISP) (Van Wart *et al.*, 2014) algorithm was used to identify the allosteric signal propagation
447 pathways through the protein. To observe conformational changes in proteins, the normal mode
448 analysis (NMA) and principal component analysis (PCA) were conducted by the ProDy program
449 (Bakan et al., 2011). In the analysis, averages were taken afterward discarding the first 200 ns
450 trajectories.

451

452 **PTEN variants mapping and visualization**

453 For variants mapping, eight PTEN mutations were considered: six in the phosphatase (Y68H,
454 H93R, A126T, R130Q, G132D, and R173C) and two in the C2 (F241S and D252G) domains. The
455 PTEN isoform structures were retrieved from the Release 42 (GRCh38.p13) of human genome on

456 the GENCODE website (<https://www.gencodegenes.org/human/>). In total, we extracted isoform
457 structures for seven PTEN isoforms. Only 5 isoforms, for which expression data was available,
458 are shown in Figure 8. When we mapped PTEN variants to the isoforms, we only considered the
459 exonic regions. The variants are grouped by the disease status (NDD vs. Non-NDD) and the two
460 groups of variants are mapped and visualized separately. To perform the variants mapping, we
461 used R language (v4.0.5) and RStudio. The Tidyverse package in R was used for data processing
462 and data analysis. To generate the schematic figure for visualization of variants mapping results,
463 we used the Gviz package in R.

464

465 **PTEN expression line plots**

466 The expression profiles of PTEN isoforms were retrieved from the BrainSpan dataset which is an
467 RNA-Seq datasets quantified at the gene and isoform levels and we downloaded it from
468 PsychENCODE Knowledge Portal, PEC Capstone Collection, Synapse ID: syn8466658
469 (<https://www.synapse.org/#!Synapse:syn12080241>). The expression data was available for 5 out
470 of 7 PTEN isoforms. For isoform expression level, transcripts per million (TPM) was used and log
471 transformed. We used R language (v4.0.5) and RStudio to perform this analysis. The Tidyverse
472 package in R was used for data processing, and the ggplot2 package in R was used for data
473 visualization.

474

475 **Figure legends**

476

477 **Figure 1.** Sequence and mutations of PTEN.

478 (A) The sequence of PTEN. In the sequence, the underlined residues highlight the mutation sites
479 in the phosphatase and C2 domains, and the phosphorylated sites in the serine-threonine cluster of
480 C-terminal tail. The residue letters are colored based on their amino acid types. (B) *In silico* model
481 of the full-length PTEN interacting with the anionic lipid bilayer composed of
482 DOPC:DOPS:PIP₂:PIP₃ (32:6:1:1, molar ratio). (C) Mapping of the residues for the mutations on
483 the PTEN structure showing the phosphatase and C2 domains. P loop containing the catalytic
484 signature motif ¹²³HCxxGxxR¹³⁰ is marked.

485

486 **Figure 2.** Y68H in the core of phosphatase domain.

487 (A) The best representative conformation from the ensemble clusters highlighting the mutation
488 site of Y68H. The wild-type PTEN is shown for comparison. In the cartoons, residues are colored
489 based on their amino acid types. In wild-type PTEN, red dotted line denotes a salt bridge. (B)
490 Violin plots representing the atomic pair distance between NZ of Lys66 in p β 3 and CG of Asp107
491 in p α 3 for Y68H and wild-type PTEN. (C) The time series of atomic pair distances between HD1
492 and HB2 of His68 for Y68H (upper panel) and Tyr68 for wild-type PTEN (lower panel). (D) The
493 allosteric pathways between the mutation site and P loop. The source residues are His68 for Y68H
494 and Tyr68 for wild-type PTEN, and the sink residues are Cys124 and Arg130 for both proteins.
495 Yellow beads represent the source and sink residues, and green beads denote the allosteric signal
496 nodes. The blue lines represent the shortest allosteric paths. The P loop is colored yellow. (E)
497 Superimpositions of the top five representative conformations of P loop for Y68H (left panel) and

498 wild-type PTEN (middle panel). Superimposition of the first representative conformations of P
499 loop from Y68H and wild-type PTEN (right panel). (F) The probability distribution of the center
500 of mass distances between the guanidine group of Arg130 and the phosphate group in the inositol
501 of PIP₃ for Y68H and wild-type PTEN.

502

503 **Figure 3.** H93R in the WPD loop.

504 Snapshot representing the best representative conformation from the ensemble clusters for H93R
505 in the anionic lipid bilayer (top left). Highlight showing the interaction of the mutant residue Arg93
506 with PIP₃ (right). The probability distribution of the center of mass distances between the
507 guanidine groups of Arg93, or Arg130 for comparison, and the phosphate group in the inositol of
508 PIP₃ for H93R (bottom left).

509

510 **Figure 4.** A126T, R130Q, and G132D in the P loop.

511 (A) The conformations of P loop and WPD loop for A126T, R130Q, and G132D. Key residues
512 are marked, and the mutated residues are marked with yellow background. (B) Violin plots
513 representing the atomic pair distance between C α of His93 in the WPD loop and C α of Arg130
514 (Gln130 for R130Q) in the P loop for A126T, G132D, and wild-type PTEN.

515

516 **Figure 5.** Water density in the active site.

517 Three-dimensional water density map with probabilities $P = 0.5$ (yellow surface) and $P = 0.4$ (blue
518 mesh) for A126T, R130Q, and G132D. Also showing wild-type PTEN for comparison. The protein
519 structures depict the best representative conformation from the ensemble clusters. The mutated
520 residues are marked with yellow background.

521

522 **Figure 6.** R173C at the interface.

523 (A) The best representative conformation from the ensemble clusters highlighting the mutation
524 site of R173C. Also showing wild-type PTEN for comparison. In the cartoons, residues are colored
525 based on their amino acid types. Yellow dotted lines denote salt bridges. (B) Violin plots
526 representing the atomic pair distance between C α of Cys173 (Arg173 for wild-type PTEN) in p α 6
527 and C α of Asp324 in the c β 7-c α 2 loop for R173C. (C) Superimposition of the first representative
528 conformations of R173C and wild-type PTEN with respect to the phosphatase domain. (D) The
529 allosteric pathways between the mutation site and P loop. The source residues are Cys173 for
530 R173C and Arg173 for wild-type PTEN, and the sink residue is Arg130 for both proteins. Yellow
531 beads represent the source and sink residues, and green beads denote the allosteric signal nodes.
532 The blue lines represent the shortest allosteric paths. The P loop is colored yellow. (E)
533 Superimposition of the first representative conformations of P loop from R173C and wild-type
534 PTEN. (F) Snapshot representing the best representative conformation from the ensemble clusters
535 for R173C. Highlight showing the interaction of PIP₃ with the C2 domain. (G) The probability
536 distribution of the center of mass distances between the guanidine group of Arg130 and the
537 phosphate group in the inositol of PIP₃ for R173C and wild-type PTEN.

538

539 **Figure 7.** F241S and D252G in the C2 domain.

540 (A) The root-mean-squared-fluctuations (RMSFs) of the C2 residues for F241S (left panel) and
541 D252G (right panel). Thin orange lines represent the RMSF of wild type PTEN for comparison.
542 (B) Averaged deviations of the amide nitrogen in the sidechains of Arg and Lys residues from the
543 bilayer surface for the PIP₃-favored residues in the phosphatase and C2 domains for F241S and

544 D252G. Also showing wild-type PTEN for comparison. Error bars denote standard deviation. (C)
545 Snapshot highlighting the hydrophobic core (surface representation in white) in the β -sandwich of
546 C2 domain for F241S and wild-type PTEN. The protein structures depict the best representative
547 conformation from the ensemble clusters. The allosteric pathways between the mutation site and
548 P loop for (D) F241S and (E) D252G. In (D), the source residues are Ser241 and Phe241 for F241S
549 and wild-type PTEN, respectively, and in (E) they are Gly252 and Asp252 for D252G and wild-
550 type PTEN, respectively. The sink residue is Arg130 for all proteins. Yellow beads represent the
551 source and sink residues, and green beads denote the allosteric signal nodes. The blue lines
552 represent the shortest allosteric paths. The P loop is colored yellow. (F) The best representative
553 conformation from the ensemble clusters highlighting the mutation site of D252G. In the cartoons,
554 residues are colored based on their amino acid types. (G) Violin plots representing the atomic pair
555 distance between Ca of Gly252 (Asp252 for wild-type PTEN) in $\text{c}\beta 5$ and Ca of Gln97 in the WPD
556 for D252G.

557

558 **Figure 8.** PTEN variants mapping and expression.

559 (A) Mapping of variants implicated in neurodevelopmental disorders (NDDs, pink) and those from
560 other diseases (green) to PTEN splicing isoforms. (B) Expression of PTEN isoforms in the
561 developing human brain for which expression levels are available. The isoform expression data
562 was quantified by the PsychEncode Consortium. Three PTEN isoforms (red, green and purple) are
563 highly expressed prenatally, and their expression levels decrease after birth. PTEN isoforms and
564 their associated exons and mutations are marked.

565

566 **Figure supplement legends**

567

568 **Figure 1–figure supplement 1.** Lipid contact probability.

569 The probability of lipid contacts for PTEN residues for (A) the phosphatase mutations (Y68H,
570 H93R, A126T, R130Q, G132D, and R173C) and (B) the C2 mutations (F241S and D252G). Also
571 showing wild-type PTEN for comparison.

572

573 **Figure 1–figure supplement 2.** Helix tilt angle of PTEN.

574 Probability distribution functions of the helix tilt with respect to the bilayer normal for helices in
575 the phosphatase domain of PTEN for (A) the phosphatase mutations (Y68H, H93R, A126T,
576 R130Q, G132D, and R173C) and (B) the C2 mutations (F241S and D252G). Also showing wild-
577 type PTEN for comparison.

578

579 **Figure 3–figure supplement 3.** Closed WPD loop conformation of PTEN H93R.

580 Violin plots representing the atomic pair distance between C α of Asp92 in the WPD loop and C α
581 of Arg130 in the P loop for H93R and wild-type PTEN (left panel). The same plots for the distance
582 between C α of Arg93 (His93 for wild-type PTEN) in the WPD loop and C α of Arg130 in the P
583 loop for H93R (right panel).

584

585 **Figure 8–figure supplement 4.** The principal component analysis (PCA).

586 The projection of the first two principal components, PC1 and PC2, for the PTEN mutations, Y68H,
587 H93R, A126T, R130Q, G132D, R173C, F241S, and D252G, and wild-type PTEN.

588

589 **Acknowledgements**

590 LMI was supported by R01MH109885 and R01MH108528. This project has been funded in whole
591 or in part with federal funds from the National Cancer Institute, National Institutes of Health, under
592 contract HHSN261201500003I. The content of this publication does not necessarily reflect the
593 views or policies of the Department of Health and Human Services, nor does mention of trade
594 names, commercial products, or organizations imply endorsement by the U.S. Government. This
595 Research was supported [in part] by the Intramural Research Program of the NIH, National Cancer
596 Institute, Center for Cancer Research. All simulations had been performed using the high-
597 performance computational facilities of the Biowulf PC/Linux cluster at the National Institutes of
598 Health, Bethesda, MD (<https://hpc.nih.gov/>).

599

600 **Author contributions**

601 H.J. built models and ran/analyzed molecular dynamics simulations. J.C. and L.M.I collected
602 genomic data and retrieved BrainSpan dataset. H.J. wrote the initial draft, and L.M.I and R.N.
603 edited the manuscript. R.N. supervised the project.

604

605 **Competing interests**

606 The authors declare no competing interests.

607

608 References

609 Abkevich, V.I., Gutin, A.M., and Shakhnovich, E.I. 1995. Impact of local and non-local
610 interactions on thermodynamics and kinetics of protein folding. *J Mol Biol* **252**, 460-471.
611 doi: 10.1006/jmbi.1995.0511.

612 Achterberg, J., Collerrain, I., and Craig, P. 1978. A possible relationship between cancer, mental
613 retardation and mental disorders. *Soc Sci Med (1967)* **12**, 135-139. doi.

614 Alvarez-Garcia, V., Tawil, Y., Wise, H.M., and Leslie, N.R. 2019. Mechanisms of PTEN loss in
615 cancer: It's all about diversity. *Semin Cancer Biol* **59**, 66-79. doi:
616 10.1016/j.semcaner.2019.02.001.

617 Bakan, A., Meireles, L.M., and Bahar, I. 2011. ProDy: protein dynamics inferred from theory and
618 experiments. *Bioinformatics* **27**, 1575-1577. doi: 10.1093/bioinformatics/btr168.

619 Bolduc, D., Rahdar, M., Tu-Sekine, B., Sivakumaren, S.C., Raben, D., Amzel, L.M., Devreotes,
620 P., Gabelli, S.B., and Cole, P. 2013. Phosphorylation-mediated PTEN conformational
621 closure and deactivation revealed with protein semisynthesis. *Elife* **2**, e00691. doi:
622 10.7554/elife.00691.

623 Bonneau, D., and Longy, M. 2000. Mutations of the human PTEN gene. *Hum Mutat* **16**, 109-122.
624 doi: 10.1002/1098-1004(200008)16:2<109::AID-HUMU3>3.0.CO;2-0.

625 Brandao, T.A., Johnson, S.J., and Hengge, A.C. 2012. The molecular details of WPD-loop
626 movement differ in the protein-tyrosine phosphatases YopH and PTP1B. *Arch Biochem
627 Biophys* **525**, 53-59. doi: 10.1016/j.abb.2012.06.002.

628 Brooks, B.R., Brooks, C.L., 3rd, Mackerell, A.D., Jr., Nilsson, L., Petrella, R.J., Roux, B., Won,
629 Y., Archontis, G., Bartels, C., Boresch, S., Caflisch, A., Caves, L., Cui, Q., Dinner, A.R.,
630 Feig, M., Fischer, S., Gao, J., Hodoscek, M., Im, W., Kuczera, K., Lazaridis, T., Ma, J.,
631 Ovchinnikov, V., Paci, E., Pastor, R.W., Post, C.B., Pu, J.Z., Schaefer, M., Tidor, B.,
632 Venable, R.M., Woodcock, H.L., Wu, X., Yang, W., York, D.M., and Karplus, M. 2009.
633 CHARMM: the biomolecular simulation program. *J Comput Chem* **30**, 1545-1614. doi:
634 10.1002/jcc.21287.

635 Busch, R.M., Srivastava, S., Hogue, O., Frazier, T.W., Klaas, P., Hardan, A., Martinez-Agosto,
636 J.A., Sahin, M., Eng, C., and Developmental Synaptopathies, C. 2019. Neurobehavioral
637 phenotype of autism spectrum disorder associated with germline heterozygous mutations
638 in PTEN. *Transl Psychiatry* **9**, 253. doi: 10.1038/s41398-019-0588-1.

639 Butler, M.G., Dasouki, M.J., Zhou, X.P., Talebizadeh, Z., Brown, M., Takahashi, T.N., Miles, J.H.,
640 Wang, C.H., Stratton, R., Pilarski, R., and Eng, C. 2005. Subset of individuals with autism
641 spectrum disorders and extreme macrocephaly associated with germline PTEN tumour
642 suppressor gene mutations. *J Med Genet* **42**, 318-321. doi: 10.1136/jmg.2004.024646.

643 Buxbaum, J.D., Cai, G., Chaste, P., Nygren, G., Goldsmith, J., Reichert, J., Anckarsater, H.,
644 Rastam, M., Smith, C.J., Silverman, J.M., Hollander, E., Leboyer, M., Gillberg, C., Verloes,
645 A., and Betancur, C. 2007. Mutation screening of the PTEN gene in patients with autism
646 spectrum disorders and macrocephaly. *Am J Med Genet B Neuropsychiatr Genet* **144B**,
647 484-491. doi: 10.1002/ajmg.b.30493.

648 Chao, J.T., Hollman, R., Meyers, W.M., Meili, F., Matreyek, K.A., Dean, P., Fowler, D.M., Haas,
649 K., Roskelley, C.D., and Loewen, C.J.R. 2020. A Premalignant Cell-Based Model for
650 Functionalization and Classification of PTEN Variants. *Cancer Res* **80**, 2775-2789. doi:
651 10.1158/0008-5472.CAN-19-3278.

652 Chau, K.K., Zhang, P., Urresti, J., Amar, M., Pramod, A.B., Chen, J., Thomas, A., Corominas, R.,
653 Lin, G.N., and Iakoucheva, L.M. 2021. Full-length isoform transcriptome of the developing
654 human brain provides further insights into autism. *Cell Rep* **36**, 109631. doi:
655 10.1016/j.celrep.2021.109631.

656 Cummings, K., Watkins, A., Jones, C., Dias, R., and Welham, A. 2022. Behavioural and
657 psychological features of PTEN mutations: a systematic review of the literature and meta-
658 analysis of the prevalence of autism spectrum disorder characteristics. *J Neurodev Disord*
659 **14**, 1. doi: 10.1186/s11689-021-09406-w.

660 Dempsey, D.R., Viennet, T., Iwase, R., Park, E., Henriquez, S., Chen, Z., Jeliazkov, J.R., Palanski,
661 B.A., Phan, K.L., Coote, P., Gray, J.J., Eck, M.J., Gabelli, S.B., Arthanari, H., and Cole,
662 P.A. 2021. The structural basis of PTEN regulation by multi-site phosphorylation. *Nat Struct Mol Biol* **28**, 858-868. doi: 10.1038/s41594-021-00668-5.

664 Fricano-Kugler, C.J., Getz, S.A., Williams, M.R., Zurawel, A.A., DeSpenza, T., Jr., Frazel, P.W.,
665 Li, M., O'Malley, A.J., Moen, E.L., and Luikart, B.W. 2018. Nuclear Excluded Autism-
666 Associated Phosphatase and Tensin Homolog Mutations Dysregulate Neuronal Growth.
667 *Biol Psychiatry* **84**, 265-277. doi: 10.1016/j.biopsych.2017.11.025.

668 Georgescu, M.M. 2010. PTEN Tumor Suppressor Network in PI3K-Akt Pathway Control. *Genes*
669 *Cancer* **1**, 1170-1177. doi: 10.1177/1947601911407325.

670 Grudzien, P., Jang, H., Leschinsky, N., Nussinov, R., and Gaponenko, V. 2022. Conformational
671 Dynamics Allows Sampling of an "Active-like" State by Oncogenic K-Ras-GDP. *J Mol*
672 *Biol* **434**, 167695. doi: 10.1016/j.jmb.2022.167695.

673 Han, S.Y., Kato, H., Kato, S., Suzuki, T., Shibata, H., Ishii, S., Shiiba, K., Matsuno, S., Kanamaru,
674 R., and Ishioka, C. 2000. Functional evaluation of PTEN missense mutations using in vitro
675 phosphoinositide phosphatase assay. *Cancer Res* **60**, 3147-3151. doi.

676 Haspel, N., Jang, H., and Nussinov, R. 2021. Active and Inactive Cdc42 Differ in Their Insert
677 Region Conformational Dynamics. *Biophys J* **120**, 306-318. doi:
678 10.1016/j.bpj.2020.12.007.

679 He, X., Ni, Y., Wang, Y., Romigh, T., and Eng, C. 2011. Naturally occurring germline and tumor-
680 associated mutations within the ATP-binding motifs of PTEN lead to oxidative damage of
681 DNA associated with decreased nuclear p53. *Hum Mol Genet* **20**, 80-89. doi:
682 10.1093/hmg/ddq434.

683 Henager, S.H., Chu, N., Chen, Z., Bolduc, D., Dempsey, D.R., Hwang, Y., Wells, J., and Cole,
684 P.A. 2016. Enzyme-catalyzed expressed protein ligation. *Nat Methods* **13**, 925-927. doi:
685 10.1038/nmeth.4004.

686 Huang, J., Rauscher, S., Nawrocki, G., Ran, T., Feig, M., de Groot, B.L., Grubmuller, H., and
687 MacKerell, A.D., Jr. 2017. CHARMM36m: an improved force field for folded and
688 intrinsically disordered proteins. *Nat Methods* **14**, 71-73. doi: 10.1038/nmeth.4067.

689 Jang, H., Banerjee, A., Chavan, T.S., Lu, S., Zhang, J., Gaponenko, V., and Nussinov, R. 2016a.
690 The higher level of complexity of K-Ras4B activation at the membrane. *FASEB J* **30**, 1643-
691 1655. doi: 10.1096/fj.15-279091.

692 Jang, H., Banerjee, A., Marcus, K., Makowski, L., Mattos, C., Gaponenko, V., and Nussinov, R.
693 2019. The Structural Basis of the Farnesylated and Methylated KRas4B Interaction with
694 Calmodulin. *Structure* **27**, 1647-1659 e1644. doi: 10.1016/j.str.2019.08.009.

695 Jang, H., Muratcioglu, S., Gursoy, A., Keskin, O., and Nussinov, R. 2016b. Membrane-associated
696 Ras dimers are isoform-specific: K-Ras dimers differ from H-Ras dimers. *Biochem J* **473**,
697 1719-1732. doi: 10.1042/BCJ20160031.

698 Jang, H., Smith, I.N., Eng, C., and Nussinov, R. 2021. The mechanism of full activation of tumor
699 suppressor PTEN at the phosphoinositide-enriched membrane. *iScience* **24**, 102438. doi:
700 10.1016/j.isci.2021.102438.

701 Jang, H., Zhang, M., and Nussinov, R. 2020. The quaternary assembly of KRas4B with Raf-1 at
702 the membrane. *Comput Struct Biotechnol J* **18**, 737-748. doi: 10.1016/j.csbj.2020.03.018.

703 Kang, H.J., Kawasawa, Y.I., Cheng, F., Zhu, Y., Xu, X., Li, M., Sousa, A.M., Pletikos, M., Meyer,
704 K.A., Sedmak, G., Guennel, T., Shin, Y., Johnson, M.B., Krsnik, Z., Mayer, S., Fertuzinhos,
705 S., Umlauf, S., Lisgo, S.N., Vortmeyer, A., Weinberger, D.R., Mane, S., Hyde, T.M.,
706 Huttner, A., Reimers, M., Kleinman, J.E., and Sestan, N. 2011. Spatio-temporal
707 transcriptome of the human brain. *Nature* **478**, 483-489. doi: 10.1038/nature10523.

708 Klauda, J.B., Venable, R.M., Freites, J.A., O'Connor, J.W., Tobias, D.J., Mondragon-Ramirez, C.,
709 Vorobyov, I., MacKerell, A.D., Jr., and Pastor, R.W. 2010. Update of the CHARMM all-
710 atom additive force field for lipids: validation on six lipid types. *J Phys Chem B* **114**, 7830-
711 7843. doi: 10.1021/jp101759q.

712 Koboldt, D.C., Miller, K.E., Miller, A.R., Bush, J.M., McGrath, S., Leraas, K., Crist, E., Fair, S.,
713 Schwind, W., Wijeratne, S., Fitch, J., Leonard, J., Shaikhouni, A., Hester, M.E., Magrini,
714 V., Ho, M.L., Pierson, C.R., Wilson, R.K., Ostendorf, A.P., Mardis, E.R., and Bedrosian,
715 T.A. 2021. PTEN somatic mutations contribute to spectrum of cerebral overgrowth. *Brain*
716 **144**, 2971-2978. doi: 10.1093/brain/awab173.

717 Kotelevets, L., Trifault, B., Chastre, E., and Scott, M.G.H. 2020. Posttranslational Regulation and
718 Conformational Plasticity of PTEN. *Cold Spring Harb Perspect Med* **10**. doi:
719 10.1101/cshperspect.a036095.

720 Lee, J.O., Yang, H., Georgescu, M.M., Di Cristofano, A., Maehama, T., Shi, Y., Dixon, J.E.,
721 Pandolfi, P., and Pavletich, N.P. 1999. Crystal structure of the PTEN tumor suppressor:
722 implications for its phosphoinositide phosphatase activity and membrane association. *Cell*
723 **99**, 323-334. doi: 10.1016/s0092-8674(00)81663-3.

724 Li, M., Santpere, G., Imamura Kawasawa, Y., Evgrafov, O.V., Gulden, F.O., Pochareddy, S.,
725 Sunkin, S.M., Li, Z., Shin, Y., Zhu, Y., Sousa, A.M.M., Werling, D.M., Kitchen, R.R.,
726 Kang, H.J., Pletikos, M., Choi, J., Muchnik, S., Xu, X., Wang, D., Lorente-Galdos, B., Liu,
727 S., Giusti-Rodriguez, P., Won, H., de Leeuw, C.A., Pardinas, A.F., BrainSpan, C., Psych,
728 E.C., Psych, E.D.S., Hu, M., Jin, F., Li, Y., Owen, M.J., O'Donovan, M.C., Walters, J.T.R.,
729 Posthuma, D., Reimers, M.A., Levitt, P., Weinberger, D.R., Hyde, T.M., Kleinman, J.E.,
730 Geschwind, D.H., Hawrylycz, M.J., State, M.W., Sanders, S.J., Sullivan, P.F., Gerstein,
731 M.B., Lein, E.S., Knowles, J.A., and Sestan, N. 2018. Integrative functional genomic
732 analysis of human brain development and neuropsychiatric risks. *Science* **362**. doi:
733 10.1126/science.aat7615.

734 Liao, T.J., Jang, H., Fushman, D., and Nussinov, R. 2020. SOS1 interacts with Grb2 through
735 regions that induce closed nSH3 conformations. *J Chem Phys* **153**, 045106. doi:
736 10.1063/5.0013926.

737 Liu, Q., Adami, H.O., Reichenberg, A., Kolevzon, A., Fang, F., and Sandin, S. 2021. Cancer risk
738 in individuals with intellectual disability in Sweden: A population-based cohort study.
739 *PLoS Med* **18**, e1003840. doi: 10.1371/journal.pmed.1003840.

740 Liu, Q., Yin, W., Meijzen, J.J., Reichenberg, A., Gadin, J.R., Schork, A.J., Adami, H.O., Kolevzon,
741 A., Sandin, S., and Fang, F. 2022a. Cancer risk in individuals with autism spectrum
742 disorder. *Ann Oncol* **33**, 713-719. doi: 10.1016/j.annonc.2022.04.006.

743 Liu, Y., Jang, H., Zhang, M., Tsai, C.J., Maloney, R., and Nussinov, R. 2022b. The structural basis
744 of BCR-ABL recruitment of GRB2 in chronic myelogenous leukemia. *Biophys J* **121**,
745 2251-2265. doi: 10.1016/j.bpj.2022.05.030.

746 Liu, Y., Zhang, M., Tsai, C.J., Jang, H., and Nussinov, R. 2022c. Allosteric regulation of
747 autoinhibition and activation of c-Abl. *Comput Struct Biotechnol J* **20**, 4257-4270. doi:
748 10.1016/j.csbj.2022.08.014.

749 Malaney, P., Pathak, R.R., Xue, B., Uversky, V.N., and Dave, V. 2013. Intrinsic disorder in PTEN
750 and its interactome confers structural plasticity and functional versatility. *Sci Rep* **3**, 2035.
751 doi: 10.1038/srep02035.

752 Malaney, R.C., Zhang, M., Jang, H., and Nussinov, R. 2021. The mechanism of activation of
753 monomeric B-Raf V600E. *Comput Struct Biotechnol J* **19**, 3349-3363. doi:
754 10.1016/j.csbj.2021.06.007.

755 Malaney, R.C., Zhang, M., Liu, Y., Jang, H., and Nussinov, R. 2022. The mechanism of activation
756 of MEK1 by B-Raf and KSR1. *Cell Mol Life Sci* **79**, 281. doi: 10.1007/s00018-022-04296-
757 0.

758 Marsh, D.J., Theodosopoulos, G., Howell, V., Richardson, A.L., Benn, D.E., Proos, A.L., Eng, C.,
759 and Robinson, B.G. 2001. Rapid mutation scanning of genes associated with familial
760 cancer syndromes using denaturing high-performance liquid chromatography. *Neoplasia*
761 **3**, 236-244. doi: 10.1038/sj.neo.7900154.

762 Meng, Z., Jia, L.F., and Gan, Y.H. 2016. PTEN activation through K163 acetylation by inhibiting
763 HDAC6 contributes to tumour inhibition. *Oncogene* **35**, 2333-2344. doi:
764 10.1038/onc.2015.293.

765 Mingo, J., Rodriguez-Escudero, I., Luna, S., Fernandez-Acero, T., Amo, L., Jonasson, A.R., Zori,
766 R.T., Lopez, J.I., Molina, M., Cid, V.J., and Pulido, R. 2018. A pathogenic role for
767 germline PTEN variants which accumulate into the nucleus. *Eur J Hum Genet* **26**, 1180-
768 1187. doi: 10.1038/s41431-018-0155-x.

769 Morris-Rosendahl, D.J., and Crocq, M.A. 2020. Neurodevelopmental disorders-the history and
770 future of a diagnostic concept. *Dialogues Clin Neurosci* **22**, 65-72. doi:
771 10.31887/DCNS.2020.22.1/macrocq.

772 Nanda, H., Heinrich, F., and Losche, M. 2015. Membrane association of the PTEN tumor
773 suppressor: neutron scattering and MD simulations reveal the structure of protein-
774 membrane complexes. *Methods* **77-78**, 136-146. doi: 10.1016/j.ymeth.2014.10.014.

775 Nordentoft, M., Plana-Ripoll, O., and Laursen, T.M. 2021. Cancer and schizophrenia. *Curr Opin
776 Psychiatry* **34**, 260-265. doi: 10.1097/YCO.0000000000000697.

777 Nussinov, R., Tsai, C.J., and Jang, H. 2022a. Allostery, and how to define and measure signal
778 transduction. *Biophys Chem* **283**, 106766. doi: 10.1016/j.bpc.2022.106766.

779 Nussinov, R., Tsai, C.J., and Jang, H. 2022b. How can same-gene mutations promote both cancer
780 and developmental disorders? *Sci Adv* **8**, eabm2059. doi: 10.1126/sciadv.abm2059.

781 Nussinov, R., Tsai, C.J., and Jang, H. 2022c. Neurodevelopmental disorders, immunity, and cancer
782 are connected. *iScience* **25**, 104492. doi: 10.1016/j.isci.2022.104492.

783 Nussinov, R., Tsai, C.J., and Jang, H. 2022d. A New View of Activating Mutations in Cancer.
784 *Cancer Res* **82**, 4114-4123. doi: 10.1158/0008-5472.CAN-22-2125.

785 Pettersen, E.F., Goddard, T.D., Huang, C.C., Couch, G.S., Greenblatt, D.M., Meng, E.C., and
786 Ferrin, T.E. 2004. UCSF Chimera--a visualization system for exploratory research and
787 analysis. *J Comput Chem* **25**, 1605-1612. doi: 10.1002/jcc.20084.

788 Phillips, J.C., Braun, R., Wang, W., Gumbart, J., Tajkhorshid, E., Villa, E., Chipot, C., Skeel, R.D.,
789 Kale, L., and Schulten, K. 2005. Scalable molecular dynamics with NAMD. *J Comput Chem* **26**, 1781-1802. doi: 10.1002/jcc.20289.

790 Pilarski, R., Burt, R., Kohlman, W., Pho, L., Shannon, K.M., and Swisher, E. 2013. Cowden
791 syndrome and the PTEN hamartoma tumor syndrome: systematic review and revised
792 diagnostic criteria. *J Natl Cancer Inst* **105**, 1607-1616. doi: 10.1093/jnci/djt277.

793 Post, K.L., Belmadani, M., Ganguly, P., Meili, F., Dingwall, R., McDiarmid, T.A., Meyers, W.M.,
794 Herrington, C., Young, B.P., Callaghan, D.B., Rogic, S., Edwards, M., Niciforovic, A.,
795 Cau, A., Rankin, C.H., O'Connor, T.P., Bamji, S.X., Loewen, C.J.R., Allan, D.W., Pavlidis,
796 P., and Haas, K. 2020. Multi-model functionalization of disease-associated PTEN missense
797 mutations identifies multiple molecular mechanisms underlying protein dysfunction. *Nat Commun* **11**, 2073. doi: 10.1038/s41467-020-15943-0.

798 Rahdar, M., Inoue, T., Meyer, T., Zhang, J., Vazquez, F., and Devreotes, P.N. 2009. A
799 phosphorylation-dependent intramolecular interaction regulates the membrane association
800 and activity of the tumor suppressor PTEN. *Proc Natl Acad Sci U S A* **106**, 480-485. doi:
801 10.1073/pnas.0811212106.

802 Redfern, R.E., Daou, M.C., Li, L., Munson, M., Gericke, A., and Ross, A.H. 2010. A mutant form
803 of PTEN linked to autism. *Protein Sci* **19**, 1948-1956. doi: 10.1002/pro.483.

804 Rodriguez-Escudero, I., Oliver, M.D., Andres-Pons, A., Molina, M., Cid, V.J., and Pulido, R. 2011.
805 A comprehensive functional analysis of PTEN mutations: implications in tumor- and
806 autism-related syndromes. *Hum Mol Genet* **20**, 4132-4142. doi: 10.1093/hmg/ddr337.

807 Ross, A.H., and Gericke, A. 2009. Phosphorylation keeps PTEN phosphatase closed for business.
808 *Proc Natl Acad Sci U S A* **106**, 1297-1298. doi: 10.1073/pnas.0812473106.

809 Sansal, I., and Sellers, W.R. 2004. The biology and clinical relevance of the PTEN tumor
810 suppressor pathway. *J Clin Oncol* **22**, 2954-2963. doi: 10.1200/JCO.2004.02.141.

811 Serebriiskii, I.G., Pavlov, V., Tricarico, R., Andrianov, G., Nicolas, E., Parker, M.I., Newberg, J.,
812 Frampton, G., Meyer, J.E., and Golemis, E.A. 2022. Comprehensive characterization of
813 PTEN mutational profile in a series of 34,129 colorectal cancers. *Nat Commun* **13**, 1618.
814 doi: 10.1038/s41467-022-29227-2.

815 Shan, L., Yu, J., He, Z., Chen, S., Liu, M., Ding, H., Xu, L., Zhao, J., Yang, A., and Jiang, H. 2020.
816 Defining relative mutational difficulty to understand cancer formation. *Cell Discov* **6**, 48.
817 doi: 10.1038/s41421-020-0177-8.

818 Shenoy, S.S., Nanda, H., and Losche, M. 2012. Membrane association of the PTEN tumor
819 suppressor: electrostatic interaction with phosphatidylserine-containing bilayers and
820 regulatory role of the C-terminal tail. *J Struct Biol* **180**, 394-408. doi:
821 10.1016/j.jsb.2012.10.003.

822 Singh, G., and Chan, A.M. 2011. Post-translational modifications of PTEN and their potential
823 therapeutic implications. *Curr Cancer Drug Targets* **11**, 536-547. doi:
824 10.2174/156800911795655930.

825 Song, M.S., Salmena, L., and Pandolfi, P.P. 2012. The functions and regulation of the PTEN
826 tumour suppressor. *Nat Rev Mol Cell Biol* **13**, 283-296. doi: 10.1038/nrm3330.

827 Spinelli, L., Black, F.M., Berg, J.N., Eickholt, B.J., and Leslie, N.R. 2015. Functionally distinct
828 groups of inherited PTEN mutations in autism and tumour syndromes. *J Med Genet* **52**,
829 128-134. doi: 10.1136/jmedgenet-2014-102803.

830 Strokach, A., and Kim, P.M. 2022. Deep generative modeling for protein design. *Curr Opin Struct
831 Biol* **72**, 226-236. doi: 10.1016/j.sbi.2021.11.008.

832

834 Tan, M.H., Mester, J., Peterson, C., Yang, Y., Chen, J.L., Rybicki, L.A., Milas, K., Pederson, H.,
835 Remzi, B., Orloff, M.S., and Eng, C. 2011. A clinical scoring system for selection of
836 patients for PTEN mutation testing is proposed on the basis of a prospective study of 3042
837 probands. *Am J Hum Genet* **88**, 42-56. doi: 10.1016/j.ajhg.2010.11.013.

838 Tan, M.H., Mester, J.L., Ngeow, J., Rybicki, L.A., Orloff, M.S., and Eng, C. 2012. Lifetime cancer
839 risks in individuals with germline PTEN mutations. *Clin Cancer Res* **18**, 400-407. doi:
840 10.1158/1078-0432.CCR-11-2283.

841 Tsou, H.C., Ping, X.L., Xie, X.X., Gruener, A.C., Zhang, H., Nini, R., Swisschelm, K., Sybert, V.,
842 Diamond, T.M., Sutphen, R., and Peacocke, M. 1998. The genetic basis of Cowden's
843 syndrome: three novel mutations in PTEN/MMAC1/TEP1. *Hum Genet* **102**, 467-473. doi:
844 10.1007/s004390050723.

845 Tu, T., Chen, J., Chen, L., and Stiles, B.L. 2020. Dual-Specific Protein and Lipid Phosphatase
846 PTEN and Its Biological Functions. *Cold Spring Harb Perspect Med* **10**. doi:
847 10.1101/cshperspect.a036301.

848 Valtcheva, N., Lang, F.M., Noske, A., Samartzis, E.P., Schmidt, A.M., Bellini, E., Fink, D., Moch,
849 H., Rechsteiner, M., Dedes, K.J., and Wild, P.J. 2017. Tracking the origin of simultaneous
850 endometrial and ovarian cancer by next-generation sequencing - a case report. *BMC
851 Cancer* **17**, 66. doi: 10.1186/s12885-017-3054-6.

852 Van Wart, A.T., Durrant, J., Votapka, L., and Amaro, R.E. 2014. Weighted Implementation of
853 Suboptimal Paths (WISP): An Optimized Algorithm and Tool for Dynamical Network
854 Analysis. *J Chem Theory Comput* **10**, 511-517. doi: 10.1021/ct4008603.

855 Waite, K.A., and Eng, C. 2002. Protean PTEN: form and function. *Am J Hum Genet* **70**, 829-844.
856 doi: 10.1086/340026.

857 Weako, J., Jang, H., Keskin, O., Nussinov, R., and Gursoy, A. 2021. The structural basis of Akt
858 PH domain interaction with calmodulin. *Biophys J* **120**, 1994-2008. doi:
859 10.1016/j.bpj.2021.03.018.

860 Xia, Q., Ali, S., Liu, L., Li, Y., Liu, X., Zhang, L., and Dong, L. 2020. Role of Ubiquitination in
861 PTEN Cellular Homeostasis and Its Implications in GB Drug Resistance. *Front Oncol* **10**,
862 1569. doi: 10.3389/fonc.2020.01569.

863 Xu, W., Yang, Z., Zhou, S.F., and Lu, N. 2014. Posttranslational regulation of phosphatase and
864 tensin homolog (PTEN) and its functional impact on cancer behaviors. *Drug Des Devel
865 Ther* **8**, 1745-1751. doi: 10.2147/DDDT.S71061.

866 Yehia, L., Ni, Y., Sadler, T., Frazier, T.W., and Eng, C. 2022. Distinct metabolic profiles
867 associated with autism spectrum disorder versus cancer in individuals with germline PTEN
868 mutations. *NPJ Genom Med* **7**, 16. doi: 10.1038/s41525-022-00289-x.

869 Yin, Y., and Shen, W.H. 2008. PTEN: a new guardian of the genome. *Oncogene* **27**, 5443-5453.
870 doi: 10.1038/onc.2008.241.

871 Zhang, M., Jang, H., Li, Z., Sacks, D.B., and Nussinov, R. 2021a. B-Raf autoinhibition in the
872 presence and absence of 14-3-3. *Structure* **29**, 768-777 e762. doi:
873 10.1016/j.str.2021.02.005.

874 Zhang, M., Maloney, R., Jang, H., and Nussinov, R. 2021b. The mechanism of Raf activation
875 through dimerization. *Chem Sci* **12**, 15609-15619. doi: 10.1039/d1sc03444h.

876 Zhang, Y., Park, J., Han, S.J., Yang, S.Y., Yoon, H.J., Park, I., Woo, H.A., and Lee, S.R. 2020.
877 Redox regulation of tumor suppressor PTEN in cell signaling. *Redox Biol* **34**, 101553. doi:
878 10.1016/j.redox.2020.101553.

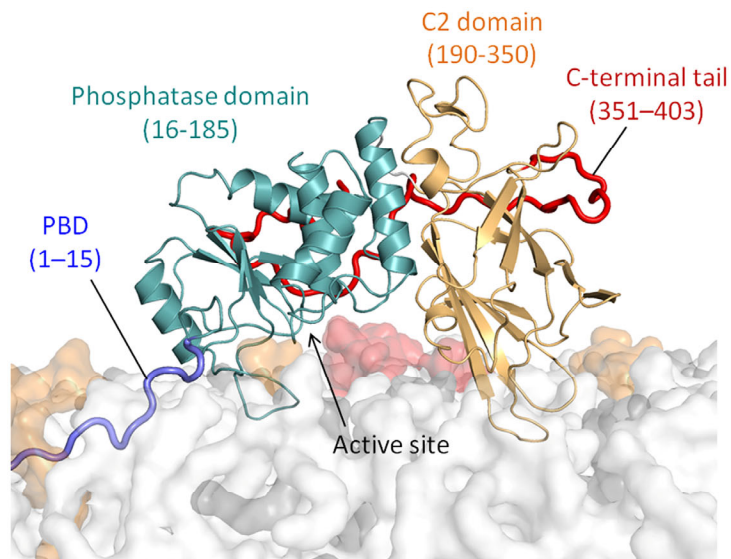
879

Fig. 1

A PTEN sequence

10	20	30	40	50	60	70	80	90	100
MTAIIKEIVS	RNKRRYQEDG	FDLDLTYIYP	NIIAMGFPAE	RLEGVYRNNI	DDVVRFLDSK	HKNHYKTYNL	CAERHYDTAK	FNCRVAQYPF	EDHNPPQLEL
110	120	130	140	150	160	170	180	190	200
IKPFCEDLDQ	WLSEDDNHVA	AIHCKAGKGR	TGVMICAYILL	HRGKFLKAQE	ALDFYGEVRT	RDKKGVTIPS	QRRYVYYYSY	LLKNHLDYRP	VALLFHKKMMF
210	220	230	240	250	260	270	280	290	300
ETIPMFSGGT	CNPQFVVCQL	KVKIYSSNSG	PTRREDKFMY	FEFPQPLPVC	GDIKVEFFHK	QNKMLKKDKM	FHF WVNTFFI	PGPEETSEKV	ENGSLCDQEI
310	320	330	340	350	360	370	380	390	400
DSICSIERAD	NDKEYLVLTL	TKNDLDKANK	DKANRYFSPN	FKVKLYFTKT	VEEPSNPEAS	SSTSVPDVS	DNEPDHYRYS	DTTDSDPENE	PFDEDQHTQI
403									
TKV									

B Membrane-bound PTEN



C Locations of key PTEN mutations

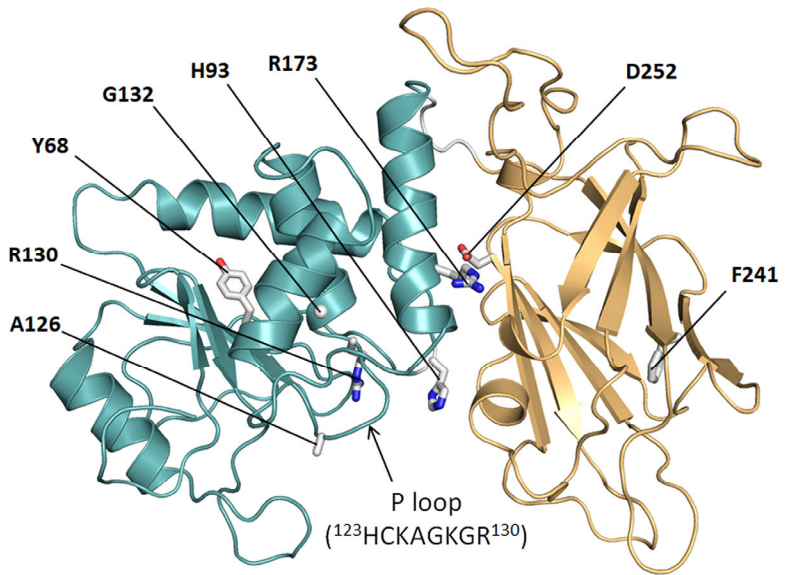
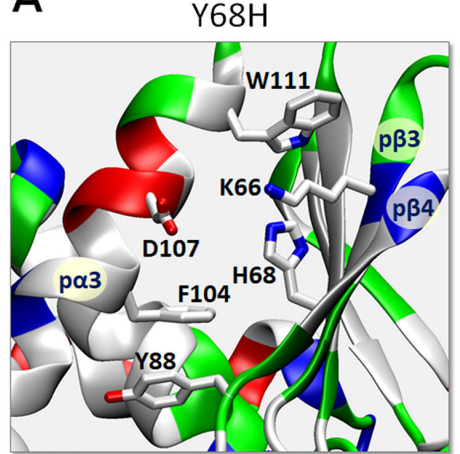
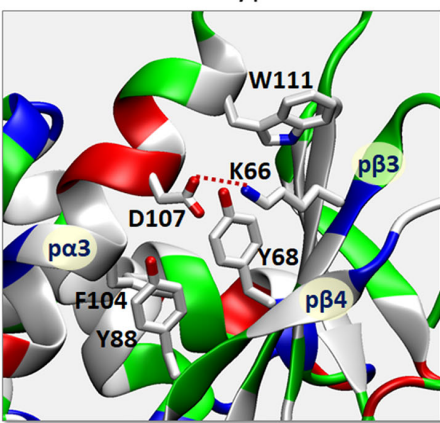


Fig. 2

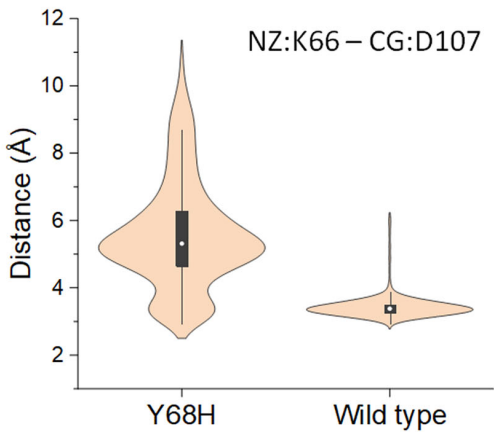
A



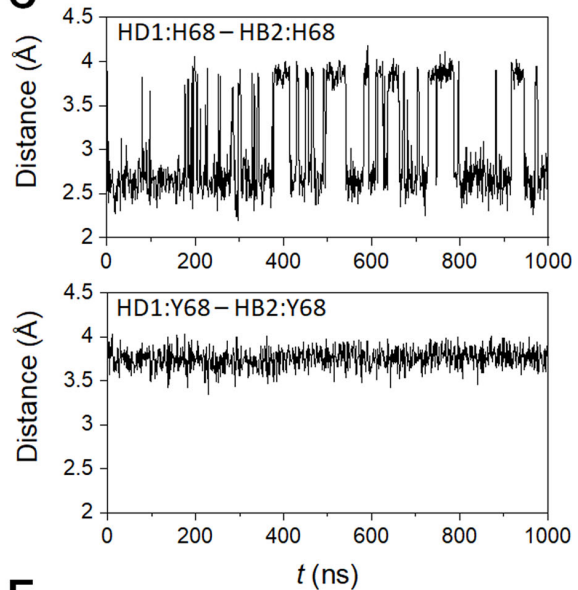
Wild type



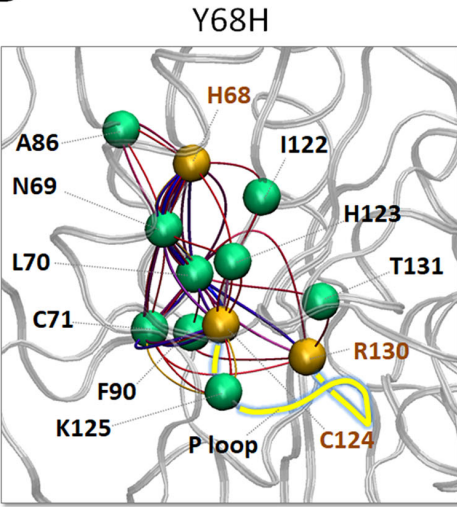
B



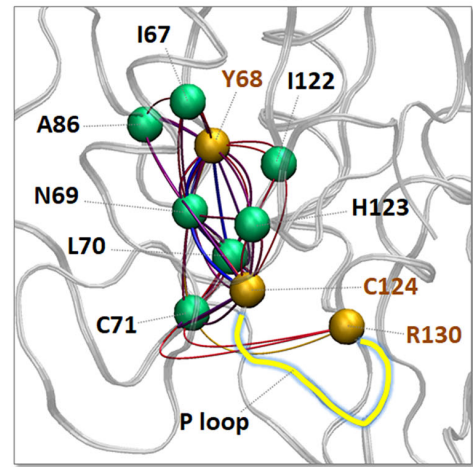
C



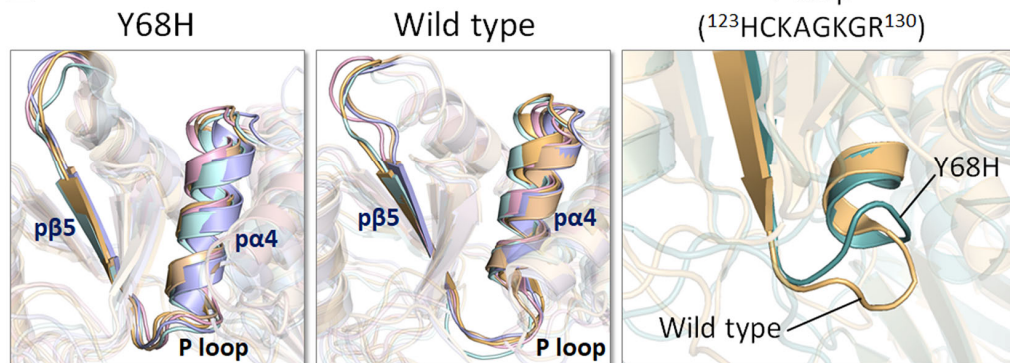
D



Wild type



E



F

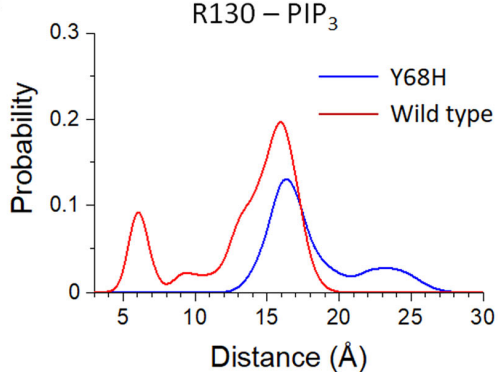


Fig. 3

H93R PTEN

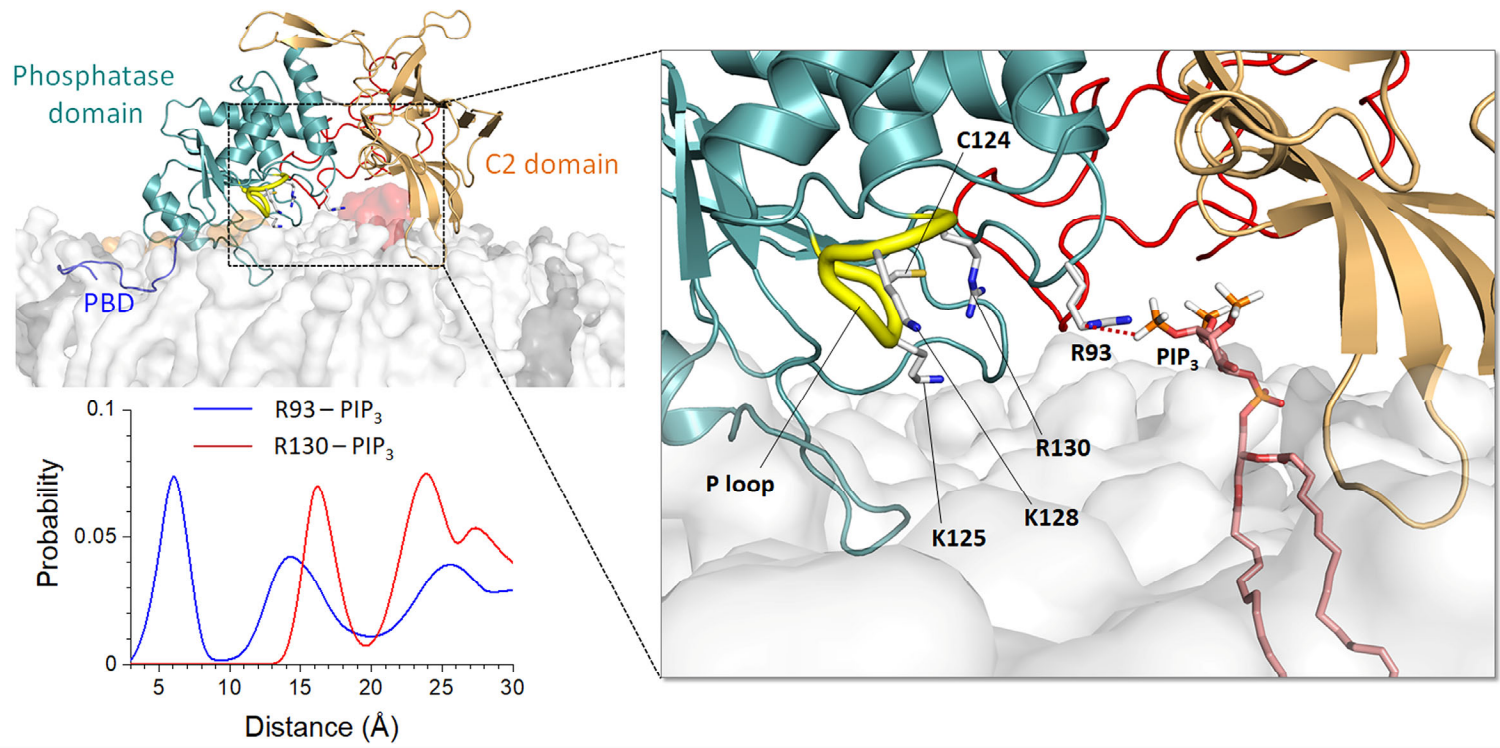
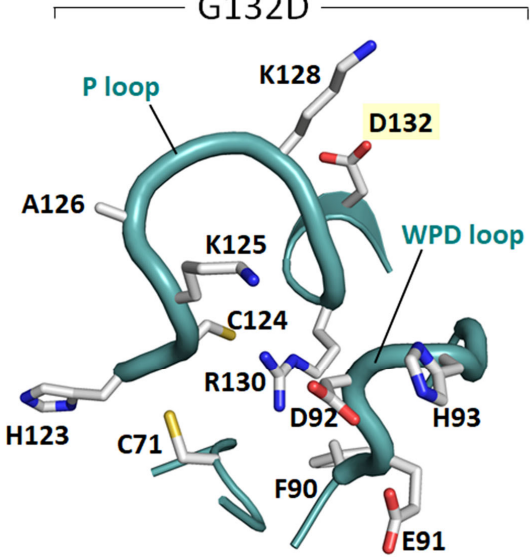
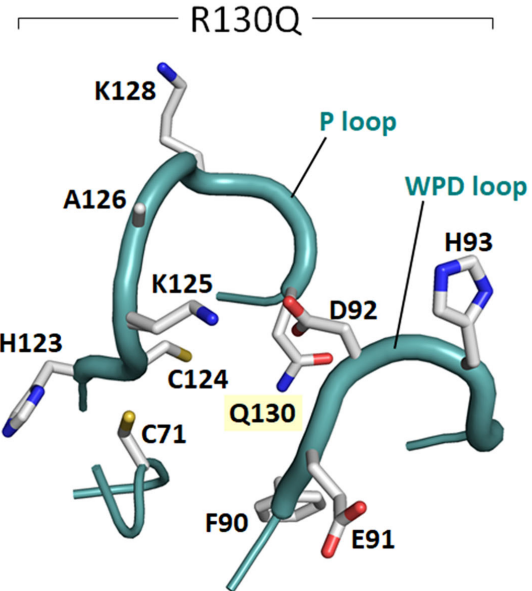
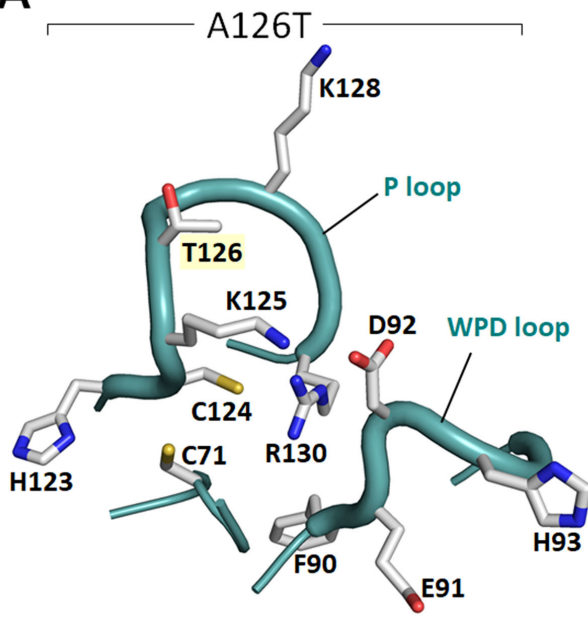


Fig. 4

A



B

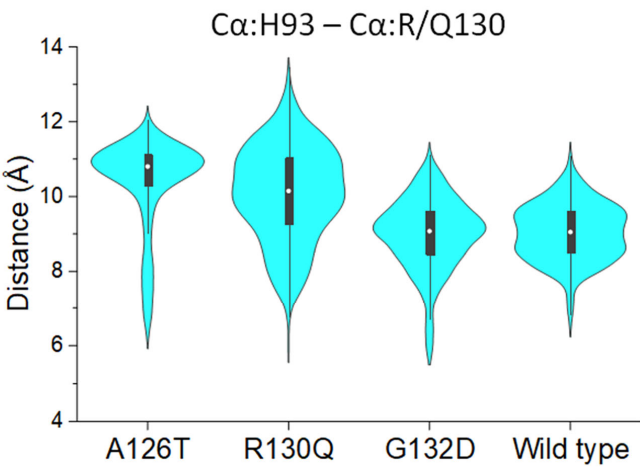


Fig. 5

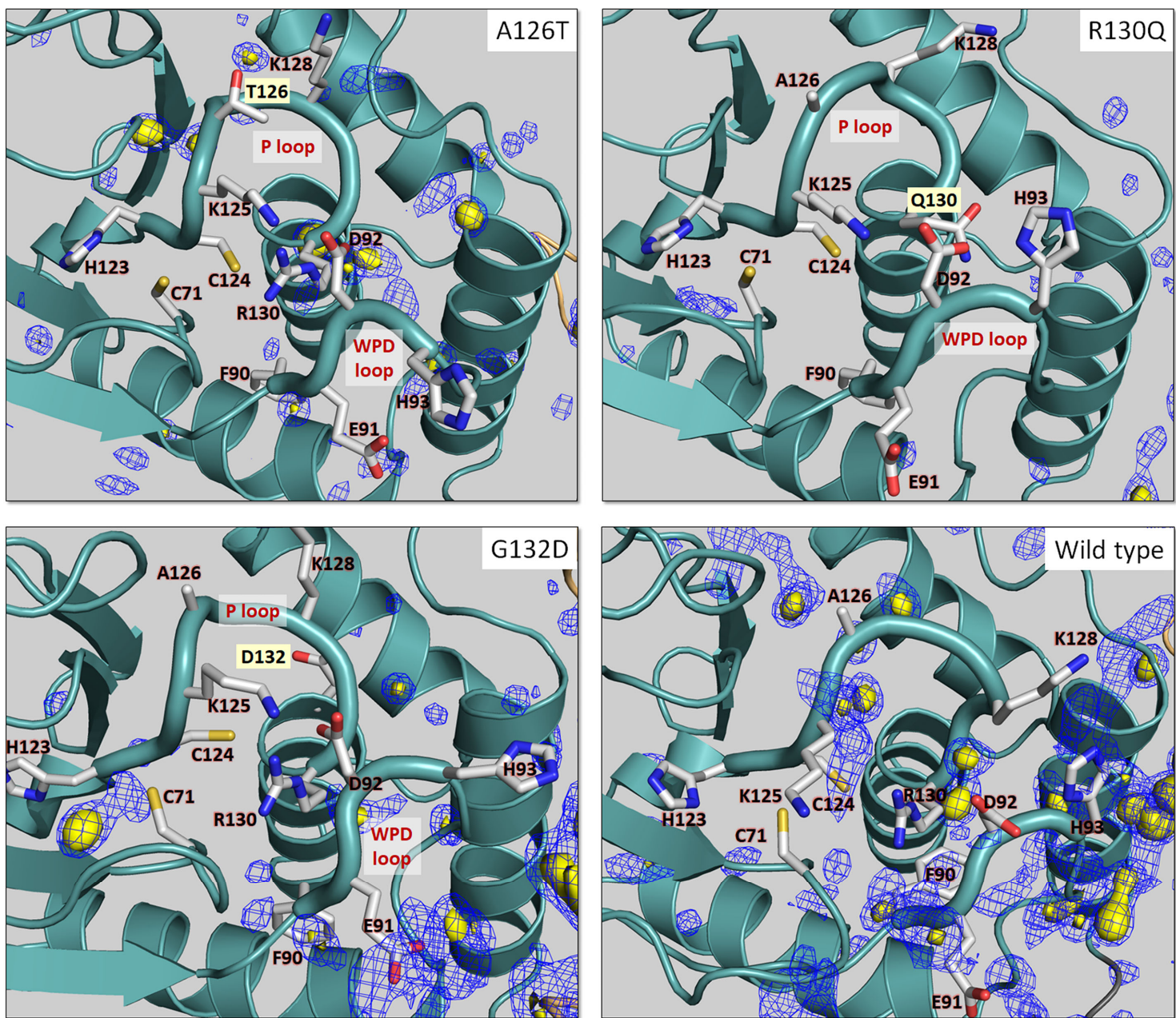
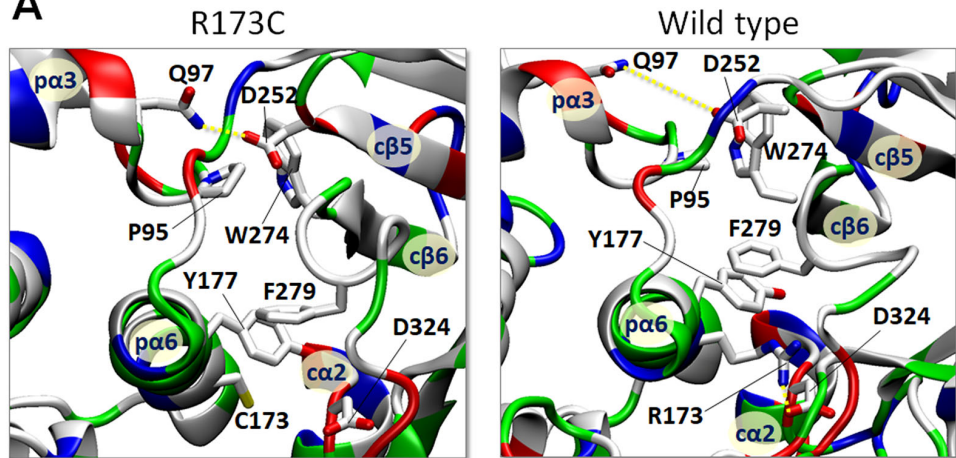
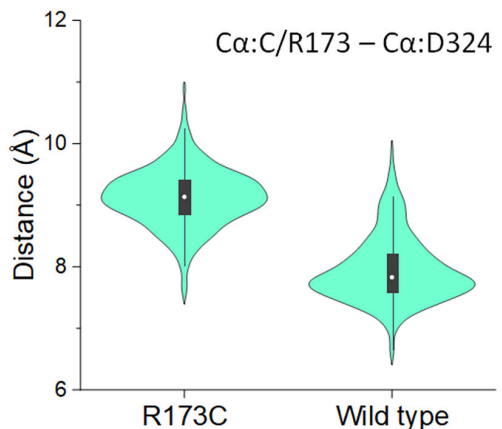


Fig. 6

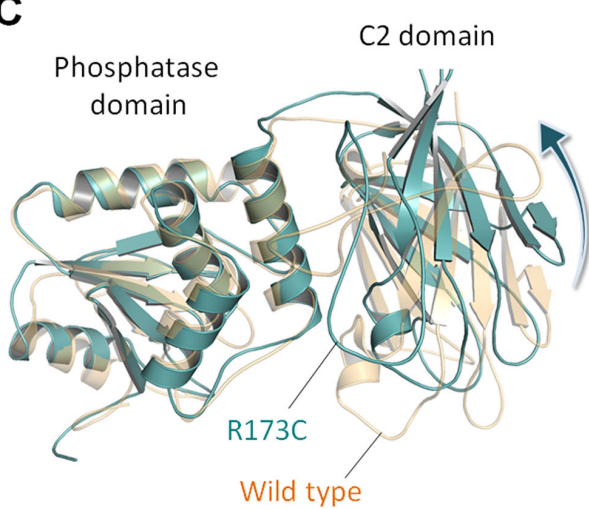
A



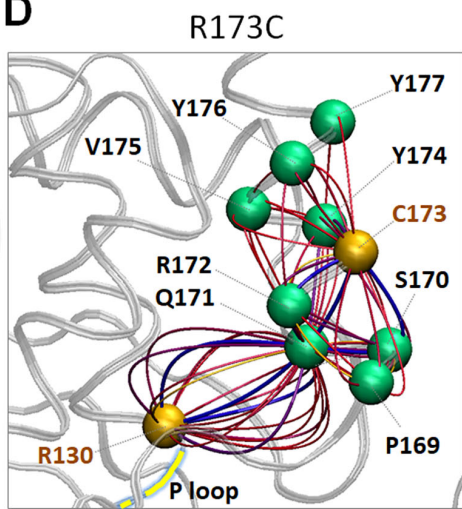
B



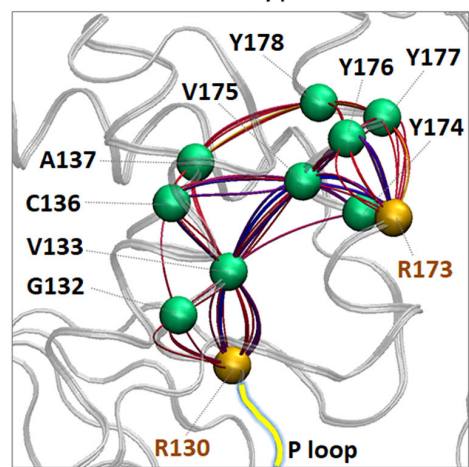
C



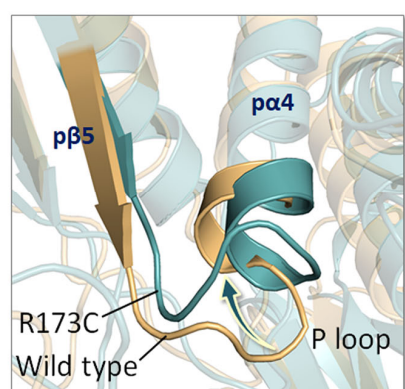
D



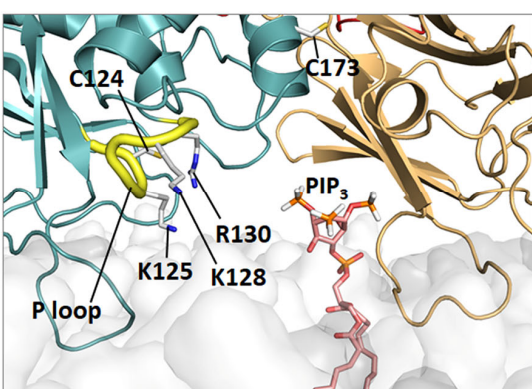
Wild type



E



F



G

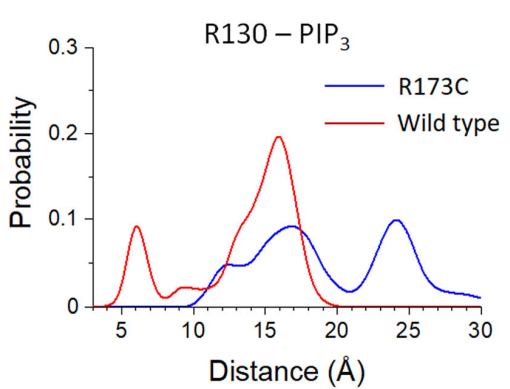


Fig. 7

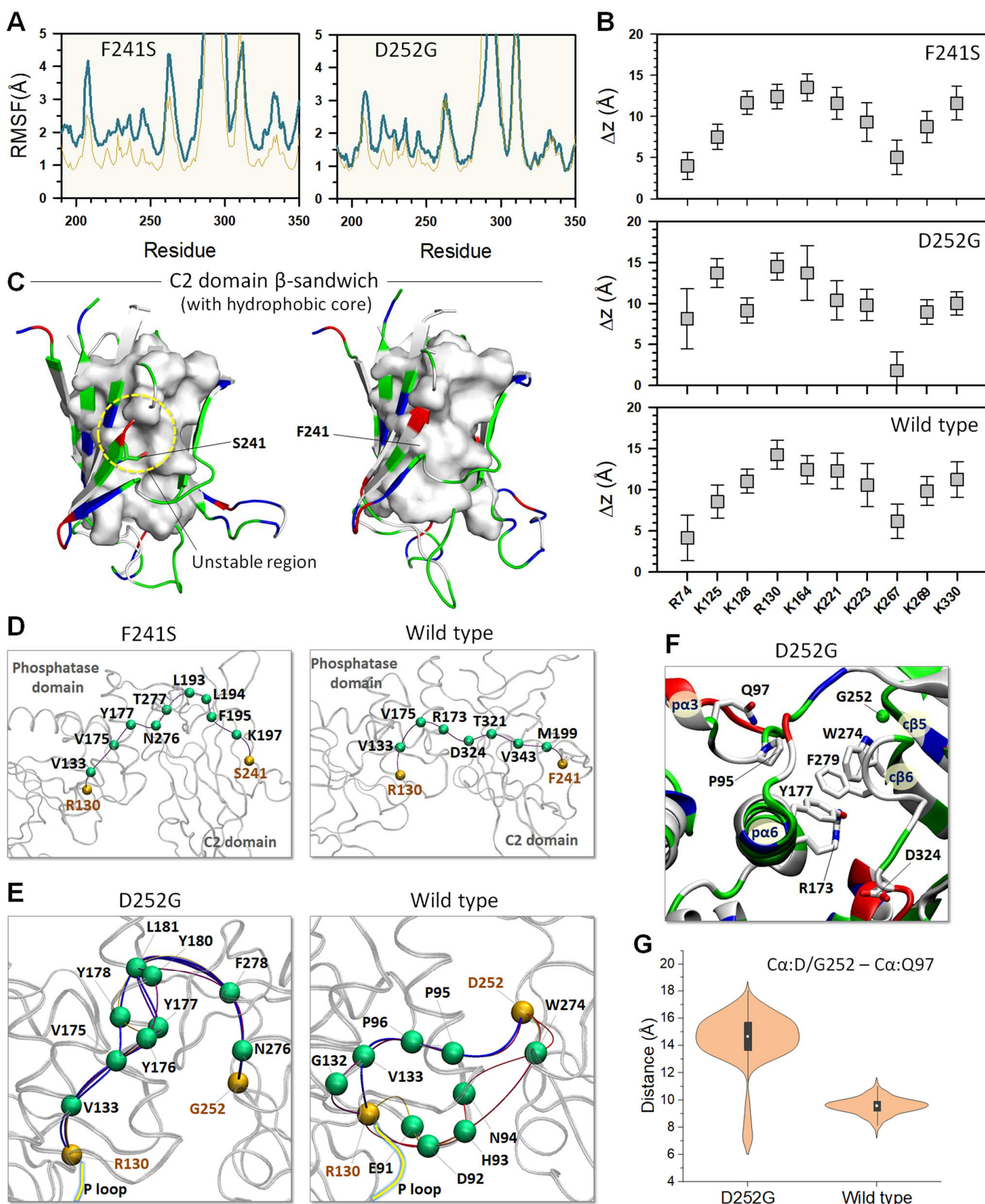
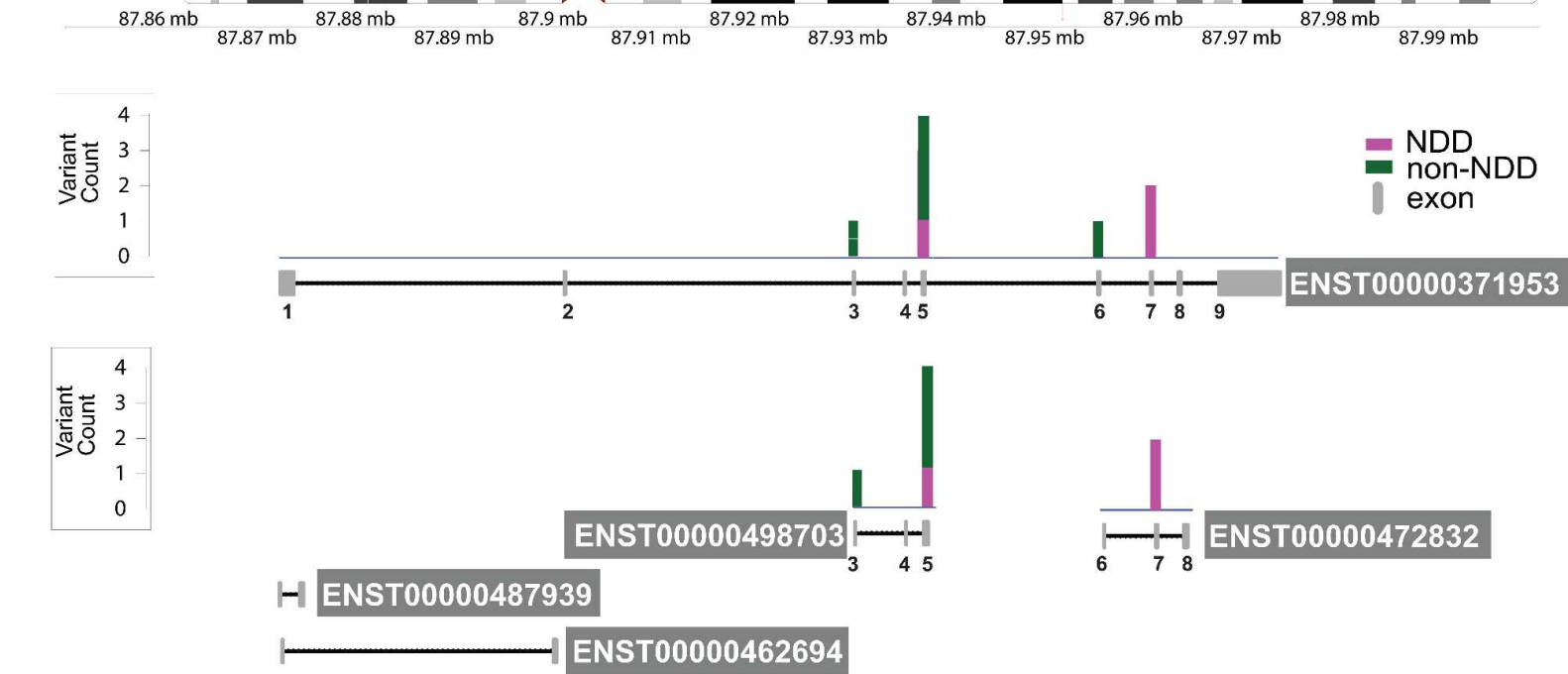


Fig. 8

A

PTEN

Chromosome



B

